Journal of Fluids and Structures 126 (2024) 104086

Contents lists available at ScienceDirect

Journal of Fluids and Structures

journal homepage: www.elsevier.com/locate/jfs

Improving predictions of vortex induced vibrations via generalizable hydrodynamic databases across several current incidence angles

José del Águila Ferrandis [a,*], Andreas Mentzelopoulos [a], Edvard Ronglan [a], Samuel Rudy [a], Dixia Fan [b], Themistoklis Sapsis [a], Michael S. Triantafyllou [a]

[a] Department of Mechanical Engineering, Massachusetts Institute of Technology, Cambridge, MA 02139, USA
[b] Department of Mechanical and Materials Engineering, Queen's University, Kingston, Ontario K7M 3N9, Canada

ARTICLE INFO

Keywords:
VIV
Riser
Optimization

ABSTRACT

Vortex induced vibrations is a withstanding ubiquitous problem in the marine industry. Although seemingly simple, cylindrical structures in cross-flows originate extremely complex and, at times, chaotic hydrodynamics which are not fully understood nowadays. One of the biggest industries driving economic development that has had to deal which this problem is Offshore Oil & Gas. Key to a safe oil extraction, marine risers have to operate and withstand the erratic process that arises from the fluid–structure interaction of marine risers with vortex induced hydrodynamic forces.

In the following paper we put forward a methodology to assimilate large amounts of data into empirical models. In doing so, we hope to bring attention to the potential that sensors and data collected by them can have in improving predictions of VIV phenomena. Although we leverage a semi-empirical VIV prediction tool (VIVA), the optimization methods used to extract robust hydrodynamic databases for a Steel Catenary Riser (SCR) are not limited to this method. The performance of the extracted databases are systematically cross-validated. To the authors' best knowledge, an extensive cross-validation of this methodology has not been performed in previous studies.

1. Introduction

Riser systems have a wide range of configuration solutions that have been used in the oil and gas industry. These systems are most commonly used for the safe transportation of material between the seabed to an offshore platform or from the platform to the seabed. Riser configurations can be divided into:

1. *Free-standing risers*: are characterized by their ability of supporting themselves as a column without a need of application of external tension.
2. *Top-tensioned risers (TTRs)*: contrary to the previous, TTRs require externally applied tension to maintain a stable structural configuration.

* Corresponding author.
E-mail addresses: jaguila@mit.edu (J. del Águila Ferrandis), ament@mit.edu (A. Mentzelopoulos), eronglan@mit.edu (E. Ronglan), shrudy@mit.edu (S. Rudy), dixia.fan@queensu.ca (D. Fan), sapsis@mit.edu (T. Sapsis), mistetri@mit.edu (M.S. Triantafyllou).

https://doi.org/10.1016/j.jfluidstructs.2024.104086
Received 16 June 2023; Received in revised form 24 December 2023; Accepted 3 February 2024

3. *Catenary risers*: characterized by the catenary shape that they adopt when they are deployed. Catenary risers made from steel pipe are called steel catenary risers or SCRs.
4. *Hybrid risers*: are assemblies that combine some or all of the previous riser concepts.

Each of the riser configurations have scenarios where they are best suited to operate. Particularly, steel catenary risers compared to top-tensioned risers offer a simpler arrangement. Usually, the riser base and tensioner can be eliminated and the deck space required is reduced. However, installation of SCRs in areas where the harshness of weather conditions is exceedingly high may not be a practical task. In these areas, where larger waves and currents appear, a significant increase of extreme loading on the riser will be experienced. This issues could be addressed with similar systems used in top tensioned risers as explained in Yin et al. (2022). However, in this cases, it is competitive advantage over these would be lost.

Early research of VIV mainly focused on the study of vibrations of rigid cylinders (Feng, 1968; Sarpkaya, 1979; Bearman, 1984). Within this research, important mechanisms of vortex induced vibrations were identified, such as hysteric behavior (Facchinetti et al., 2004) or lock-in phenomena (Dahl et al., 2010). However, for oil and gas, industrial development long flexible cylinders must be understood and designed reliably. Research of VIV of long flexible risers is composed mainly of physical experiments (Song et al., 2011; Gao et al., 2015; Xu et al., 2017; Chaplin et al., 2005; Trim et al., 2005; Huera-Huarte and Bearman, 2009; Gedikli et al., 2018, 2017) and numerical computations (Newman and Karniadakis, 1997; Evangelinos and Karniadakis, 1999; Bourguet et al., 2011, 2012, 2013). Most of these studies focus on conditions where the risers do not undergo large displacements from a straight line and are not subject to large variations in their effective tension or in their effective length. These studies have been essential to enable the development and validation of numerical codes that are capable of predicting fatigue of deep water risers offshore. However, further research is needed to match the understanding of straight risers when it comes to riser and umbilical geometries that have large curvature, variation of tension along their length and/or are inclined to various angles with respect to the flow. As found by Chaplin and King (2018), untensioned catenary risers tend to present a higher bandwidth in their response than tensioned risers perpendicular to the flow. Examples of research that has been done to understand non-straight riser geometries include yawed cylinders (King, 1977; Ramberg, 1983), spring-mounted rigid/flexible cylinders in yawed/sheared flow (Jain and Modarres-Sadeghi, 2013; Zhu et al., 2021) and rigid cylinders with curved axis (Miliou et al., 2007). Given the importance of quantifying fatigue at the touch down point, focus has been drawn by Kim et al. (2006) and Wang et al. (2015b), where hard and soft sea floors are considered. The lack of pretension in steel catenary risers allow for larger vessel motions that can potentially couple with the riser dynamics as shown by Chatjigeorgiou et al. (2008), Pereira et al. (2013), Wang et al. (2015a, 2014, 2017).

Recently, semi-empirical methods have been widely adopted to predict VIV of long flexible structures. Semi-empirical methods, instead of calculating hydrodynamic forces by resolving Navier–Stokes equations, leverage rigid cylinder experiments. Furthermore, semi-empirical methods can be further divided into those that use experiment data directly to model hydrodynamic forces (Triantafyllou, 1998; Larsen et al., 2001; Vandiver and Li, 2005; Zheng et al., 2011a) and those that model hydrodynamic forces non-linear oscillators (Facchinetti et al., 2004; Farshidianfar and Zanganeh, 2010). Existing semi-empirical codes address cross-flow oscillations only.

Vortex induced vibrations can affect any of the previously mentioned riser configurations. VIV, if not considered in the design process of the riser, can seriously compromise the structural integrity when severe fatigue (Baarholm et al., 2006) results in catastrophic failure of the structure, causing severe economic and, maybe more importantly, severe environmental consequences.

With this in mind, in this paper we put forward a significant extension of the methodology presented in Rudy et al. (2021) to characterize the VIV vibrations of a SCR riser in unseen conditions, both interpolated and extrapolated. We use data collected in controlled lab experiments (Braaten and Lie, 2004) by extracting hydrodynamic databases with a semi-empirical method (VIVA Zheng et al., 2011a). The validity of the databases obtained, and hence the methodology, is then assessed by predicting VIV response in sets of unseen cases during the database extraction. During the methodology assessment, we neglect some features. Most importantly, the effect of the curvature (Hover and Triantafyllou, 1999; Lu, 1994; Yin et al., 2019) of the catenary riser on the modes of vibration. However, given that the focus of the study is to evaluate the methodology robustness, we believe we can say that the neglected features do not invalidate the assessment. Notably, our methodology demonstrates improvements in predictions compared to those based on standard databases, as can be seen in Figs. 6 to 8. These enhancements are evident in more accurate and consistent predictions across various conditions, showcasing the potential of our approach in advancing hydrodynamic database optimization and VIV prediction accuracy.

A key aspect of our methodology is the incorporation of physics-informed choices for constraining the bounds of hydrodynamic coefficients. By integrating fundamental physical principles into the learning process, we are able to define more realistic and meaningful bounds for these coefficients. This approach not only improves the learning efficiency and generalization capabilities of our model but also ensures that the predictions are physically plausible and adhere to known hydrodynamic behaviors. The consequence of this approach is a significant enhancement in the reliability and applicability of the hydrodynamic databases, especially in scenarios where direct experimental data might be limited or unavailable. This advancement represents a substantial step forward in the field of VIV modeling, opening new avenues for optimized design and analysis of marine structures under complex fluid dynamic conditions.

2. Description of the experiments

The experimental program, as detailed in the report (Braaten and Lie, 2004), involved an extensive model test to gather experimental data on the Vortex-Induced Vibration (VIV) response of a Steel Catenary Riser (SCR), see A.10. The key characteristics of these experiments are summarized as follows:

- **Riser Model**: The tests utilized a catenary riser model with a length-to-diameter ratio of approximately 900. The model was constructed from brass pipe and equipped with accelerometers for vibration measurement.
- **Test Setup**: The riser model was towed in a towing tank, allowing for systematic variation of both current velocity and inclination angle between the current and the riser.
- **Measurement Techniques**: The VIV response was primarily measured using 10 pairs of accelerometers strategically placed along the riser. These instruments captured detailed data on riser motion in response to varying current conditions.
- **Test Conditions**: A range of tests were conducted to simulate different scenarios, including varying current velocities and directions relative to the riser (see Table 1). This approach provided a comprehensive set of data to analyze VIV behavior under diverse conditions.

This rigorous experimental setup and the resultant data were crucial in developing and validating the predictive model for VIV in SCRs, particularly under varying flow conditions. The detailed experimental approach provided a robust foundation for the predictive methodologies discussed in our manuscript.

3. Methodology

The VIV amplitude and frequency prediction is performed assimilating the SCR riser to a straight riser, where the tension of the riser is the mean tension over the SCR riser and the CF and IL components are defined from the perpendicular component of the water velocity to the longitudinal direction along the riser. The tangential component is discarded for any VIV calculations. This is a simplification of the varying tension along the riser and the varying incidence angle of the flow generates different current profiles. Furthermore, since the system has not got a pretension, such as straight risers, ballooning effects can considerably change the shape of the riser, changing the incidence angle of the flow and adding complexity to the problem. Ballooning of a Steel Catenary Riser (SCR) refers to the deformation and expansion of the riser due to changes in internal pressure and temperature. This phenomenon causes the riser to radially and axially expand, leading to increased stress and potential structural challenges.

The assumptions that we put forward in the previous paragraph are strong, as previous studies have shown that the axial component of the flow velocity can add riser tension. Ballooning effects can change the geometry of the riser significantly and making necessary to account for them in the VIV predictions. Nevertheless, for the particular flow conditions that are considered in this study, the assumptions provide good performance (see Figs. 6 to 8) and allow for significant improvement over standarized databases that provide conservative predictions that typically overpredict by 40% VIV response of marine risers. This is mainly because they are usually based on databases extracted in rigid cylinder experiments. With this in mind, we put forward a methodology, to obtain from sensors, generalizable hydrodynamic databases to improve predictions for a wide range of methods.

3.1. Flexible cylinder VIV

By using a strip theory approach (Fan et al., 2019), the free vibrations of a flexible cylinder within a current profile can be predicted using rigid cylinder experimental data. Particularly, for a vertical flexible cylinder, denoting z as the vertical axis, the cylinder spans $z = 0$ and $z = L$. Considering μ the mass per unit length, c the structural damping per unit length, EI the bending stiffness, T the tension at the top, and $\mathcal{F}_l(z,t)$ the fluids time-varying fluid lift force per unit length in the Cross Flow (CF) direction at the span-wise location z, considering small amplitude of vibration, the structural model can be expressed as:

$$\mu\frac{\partial^2 y}{\partial t^2} + c\frac{\partial y}{\partial t} - \frac{\partial}{\partial z}(T\frac{\partial y}{\partial z}) + \frac{\partial^2}{\partial z^2}(EI\frac{\partial^2 y}{\partial z^2}) = \mathcal{F}_l(z,t) \tag{1}$$

Just like a rigid cylinder, the riser's monochromatic steady oscillation is $y(z,t) = Re\left\{Y(z)e^{i\omega t}\right\}$. $Y(z)$ is the complex space-dependent amplitude of oscillation with frequency ω. The lift force $\mathcal{F}_l(z,t)$ is expressed as:

$$\mathcal{F}_l(z,t) = Re\{[C_{my}\rho_f \forall Y(z)\omega^2 + iC_{lv}\frac{\rho_f U^2}{2}D\frac{Y(z)}{|Y(z)|}]e^{i\omega t}\} \tag{2}$$

Substituting Eq. (2) in Eq. (1) leads to a nonlinear eigenvalue problem:

$$[-\omega^2(m + C_{my}\forall) + i\omega b]Y - \frac{\partial}{\partial z}(T\frac{\partial Y}{\partial z}) + \frac{\partial^2}{\partial z^2}(EI\frac{\partial^2 Y}{\partial z^2}) = iC_{lv}\frac{\rho_f U^2}{2}D\frac{Y}{|Y|} \tag{3}$$

As seen previously, C_{my} and C_{lv} are functions of A^*, $V_r = \dfrac{1}{f_r}$ and Re, which can be obtained in the hydrodynamic databases of rigid-cylinder, CF-only forced vibrations. Semi-empirical codes such as VIVA (Triantafyllou et al., 1999) are used to solve Eq. (3).

3.2. Parametric hydrodynamic databases

Accurate C_m and C_{lv} databases have the ability to capture dependencies of large amount of independent variables such as structural and flow parameters. This requires a large amount of experimental data, which usually need large and expensive experimental setups to study full scale Reynolds numbers. Dependencies on other parameters surface roughness and other properties that may change over time makes the problem of obtaining universal databases impractical if not intractable.

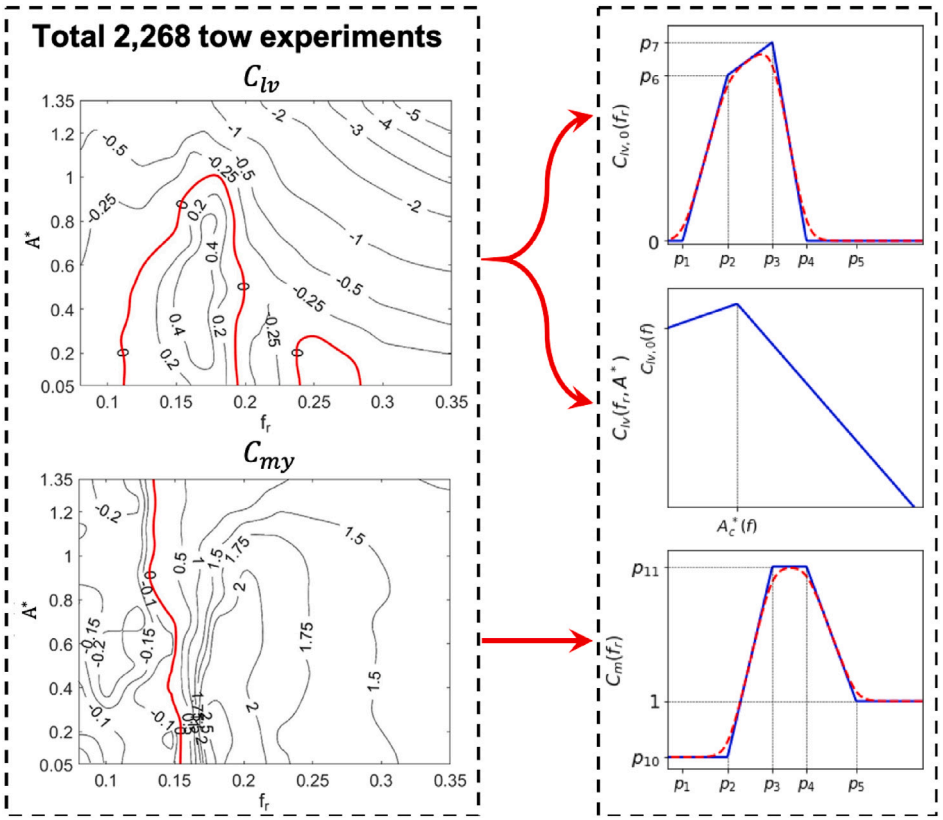

Fig. 1. On the left, an example of a hydrodynamic coefficient database reconstructed from a large number of tow experiments (Rudy et al., 2021). From it, we make informed decisions as to what are good simple parametric representations to approximate C_{lv} and C_{my} from field or experimental data (right).

In this work, we evaluate extrapolation and interpolation of databases obtained using the method proposed in Rudy et al. (2021) to unseen flow conditions during the extraction of the hydrodynamic database. With this exercise, we hope to see if we can obtain reliable predictions even in these unseen flow conditions, to have an evaluation of the robustness of the method.

Parametric forms for both C_m and C_{lv} are used. This approach captures salient and dynamically-relevant features. These parametric forms may then be used in tandem with the known governing equations for VIV and numerical solvers to obtain predictive models. Comparing with experimental results for particular structures leads to an optimization problem first put forward by Mukundan (2008). The parametric databases used in this work are informed by the experimental results obtain by the Norwegian Deep Water Program (NDP).

Taking an informed decision by looking at experimental evidence, C_{my} is considered only dependent on f_r. This is done considering 3 regimes of constant C_{my} separated by linear transitions (Fig. 1), where smoothed soft-plus functions are used to provide smooth transitions. Furthermore, C_{lv} is approximated by another piece-wise linear function of the amplitude of oscillation. The starting point of C_{lv}, $C_{lv,0}(f_r)$, is approximated also piece-wise linearly and the transition zones are also smoothed soft-plus functions.

The resulting hydrodynamic model has 14 variables. Five of them are values of reduced frequency, that set the transition zones between the different regimes which are shared between C_{my}, $C_{lv,0}$, and A_c^*. For each C_{my}, $C_{lv,0}$, and A_c^* two additional parameters are used to specify the slopes C_{lv} as function of the amplitude.

3.3. Predicting the structural response

3.3.1. Database optimization for risers

For flexible cylinders, the assumption of harmonic motion yields the non-linear eigenvalue problem given by Eq. (3), which depends on the hydrodynamic databases for C_{lv} and C_{my}. We follow the approach first considered in Mukundan (2008) for learning optimal databases and solve Eq. (3) using the semi-empirical code VIVA (Triantafyllou et al., 1999). This yields a map from prescribed flow parameters to $\hat{A}^*(z;\mathbf{p})$, $\hat{f}_{peak}(\mathbf{z})$, which are predictions for multi-modal amplitude and peak frequency made by the

Table 1
Experiment labels and cells colored in red for test and blue for train. The table above corresponds to training on current directions (ϕ) 30°, 60° & 90° and testing on 0°.

Current velocity (m/s)	Dir. 0 deg.	Dir. 30 deg.	Dir. 60 deg.	Dir. 90 deg.
0.12	1000 & 5001	2004	3000	4000
0.14	1002	2001	3002	4002
0.16	1004	2002	3004	–
0.18	1006	2006	3006	4006
0.20	1008	2008	3008	4008
0.22	1010	2010	3010	–
0.24	1012 & 5012	2012	3012	4012
0.26	1015	2015	3015	–
0.28	1016	2016	3016	–
0.30	1018 & 5018	2018	3018	4018
0.32	1020	2020	3020	4020
0.34	1022 & 5022	2022	3022	4022

semi-empirical code VIVA. The parameters are extracted from experimental data using the process outlined in Appendix A. We define the objective function as,

$$J(\mathbf{p}) = \sum_{(A^*(z),f_{peak})\in D} \left(\frac{1}{L} \int_0^L |A^*(z) - \hat{A}^*(z;\mathbf{p})|^2 \, dz \right)^{\frac{1}{2}} + \lambda |f_{peak} - \hat{f}_{peak}(\mathbf{z})|, \tag{4}$$

where $A^*(z)$ and $f_{peak}(\mathbf{z})$ are experimentally measured values contained in a dataset D sampled at different flow velocities.

$$\hat{\mathbf{p}} = \underset{\mathbf{p}}{argmin}\, J_f(\mathbf{p}) + \mathcal{R}(\mathbf{p}), \tag{5}$$

$\mathcal{R}(\mathbf{p})$ represents regularization terms that imposes a penalty on the size of the range of reduced frequencies, $\hat{f}_r$, whose C_{lv} has positive values $(p_4 - p_1)$; the range of $\hat{f}_r$ where C_{my} does not take constant values, $(p_5 - p_2)$ and the greatest value of A^* on the zero contour of C_{lv}, see Appendix C for full definition. These penalties where used by Rudy et al. (2021) and were shown to lead to more plausible results, although the end effect is small.

In this work, we select a dataset obtained in the Norwegian Deepwater Program (NDP) large-scale laboratory experiments. The data were obtained from a 12.5 m uniform SCR riser placed within a uniform current with incoming velocity ranging from 0.12 m/s to 0.34 m/s. The details of the NDP experiment and the corresponding dataset are described in Appendix A.

3.4. Optimization routine

The loss function employed in this research has an irregular behavior that include plateaus, which make the choice of descent direction as well as the step size particularly challenging using line search. The best results were obtained by evaluating the cost function at random perturbations. More specifically, in iterative fashion, we set $\mathbf{p} = \mathbf{p} + \delta_i \mathbf{v}_i$ where:

$$\delta_i = \underset{\delta\in\Delta}{arg\,min}\, J(\mathbf{p} + \delta\mathbf{v}_i) + \mathcal{R}(\mathbf{p} + \delta\mathbf{v}_i), \tag{6}$$

In the previous equation, $\Delta = \{0, \delta_1, \dots, \delta_{n_{samp}}\}$ including 0 and n_{samp} samples distributed according to p_δ, $\mathbf{v}_i$ is a search direction.

Previous work (Rudy et al., 2021), has found coordinate descent to have superior performance on Eq. (5). Other tested approaches in Rudy et al. (2021), which have been successfully applied to similar problems, are Nelder–Mead algorithm and simulated annealing. The implemented coordinate descent algorithm iterates through every dimension of $\mathbf{p}$ to solve the one dimensional problem given by:

$$p_i = \underset{y}{argmin}\; J(p_1, \dots, p_{i-1}, y, p_{i+1}, \dots) + \mathcal{R}(p_1, \dots, p_{i-1}, y, p_{i+1}, \dots). \tag{7}$$

Eq. (5) is more easily solved after multiple trials of the optimization scheme if computational resources allow, as it is non-convex.

4. Methodology robustness through cross-validation

In our effort to robustly assess the hydrodynamic databases extracted using the method outlined in Section 3, we follow standard AI methodologies for model validation. This approach involves cross-validation of the model across four different current directions, thereby ensuring that the training is not merely curve-fitting but is genuinely generalizable. For this, part of the experimental data is used to train the model, while the remainder is employed to test the model, focusing on vortex induced vibrations in SCR. An illustrative example of the training and testing cases for the first set of data is provided in Table 1.

The chosen format of cross-validation is designed to evaluate the model's predictive capabilities in conditions beyond those observed during training, specifically for extrapolating and interpolating flow conditions. This strategy is key to updating existing databases and expanding their parametric range applicability. A demonstration of the model's excellent generalization properties, achieved by this methodology, is evident in the performance displayed in Figs. 2 and 5 . This approach ensures that our model extends beyond simple curve-fitting, offering reliable predictions for a wide range of parameters.

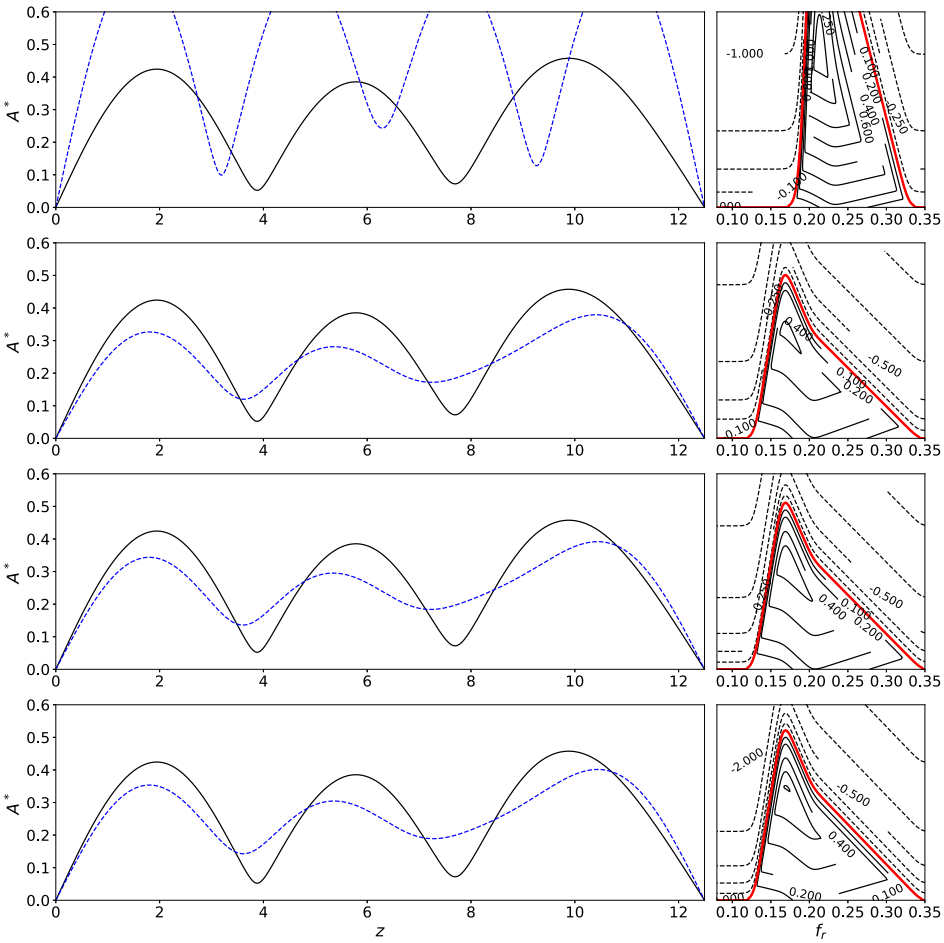

Fig. 2. Test case 1000. *Cross flow RMS predictions, testing catenary plane angle with velocity* $\phi = 0°$. Solid black curve are reconstructed displacements and blue-dashed line are optimized VIVA predictions. A single hydrodynamic database is used. In this figure we represent the change in spanwise RMS response as the training is performed in the 3 catenary plane orientations to which this specific case does not belong to, in this particular case $\phi = 30°, 60°, 90°$. For the relation between experiment labels and catenary plane orientations & towing velocities Table 1 can be consulted. (For interpretation of the references to color in this figure legend, the reader is referred to the web version of this article.)

5. Results and discussion

The final results of the cross-validation study are presented in Figs. 2 to 5 and Figs. D.15 and D.16, these last two in Appendix D. In Figs. 2 to 5 we present four graphs stacked vertically. In each of them a blue dashed line is plotted alongside a solid black line. They correspond to the span-wise RMS of CF Amplitude predicted by VIVA and the experimental data, respectively. The top-most graph corresponds to initial state of the hydrodynamic database obtained after fifty random draws of the parametric database. Although the method we put forward is meant to improve existing databases, we perform random draws to evaluate the effect of starting the optimization from different start points, and further assess the robustness of the methodology. Stacked below the previous graph are three graphs that show the same information as the previous at different stages of the training process. This is done for the cases which are left out of the training phase. In other words, Figs. 2 to 5 are visualizations of the testing VIV predictions as the training develops.

The overall training and testing errors are provided in Figs. D.15 and D.16. These figures illustrate that a reduction in training error is consistently followed by a reduction in test error for almost all cases. This positive correlation between training and testing performances signifies that as the model's accuracy improves during the training phase, these enhancements are effectively mirrored in the testing phase, indicating a well-behaved generalization of the predictive capabilities of the parametric databases. This trend is a crucial indicator of the model's generalizability, suggesting effective learning of underlying patterns applicable to unseen data, and is the main result we aimed to prove.

However, the figures also reveal that certain catenary plane orientations yield better predictions than others. Most notably, for $\phi = 90°$, both training and testing errors are larger compared to other catenary plane angles. This could be attributed to the absence

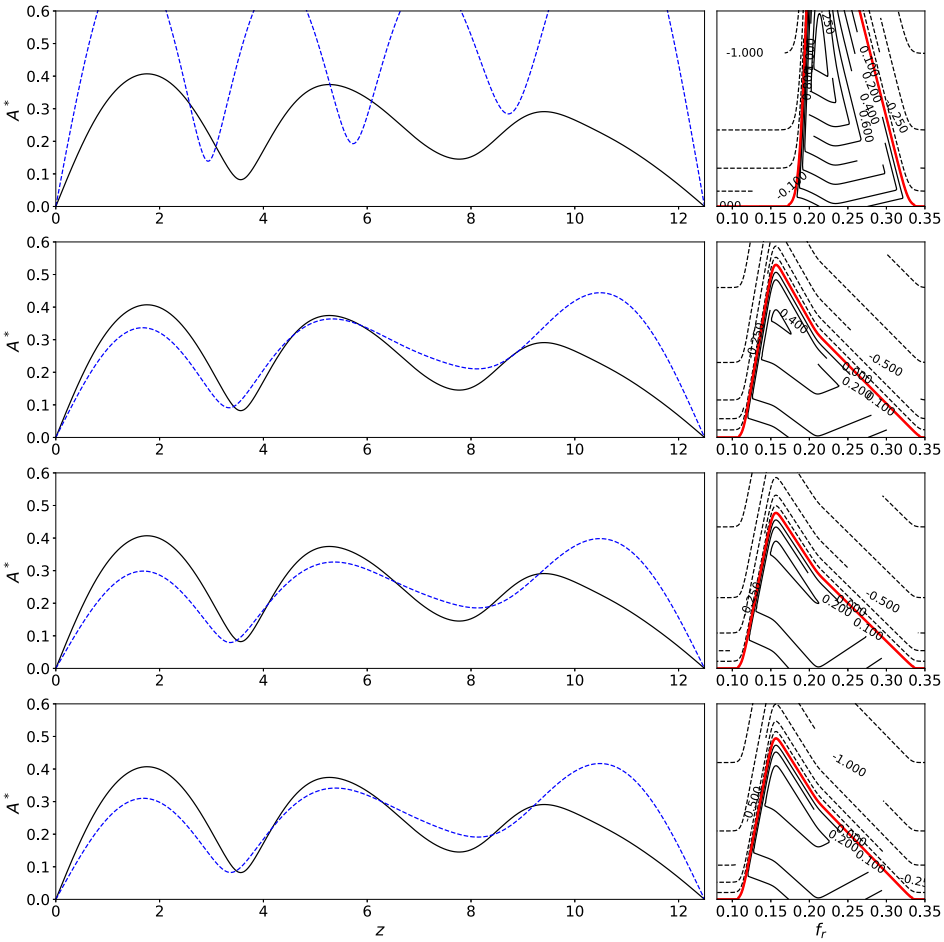

Fig. 3. Test case 2001. *Cross flow RMS predictions, testing catenary plane angle with velocity* $\phi = 30°$. Solid black curve are reconstructed displacements and blue-dashed line are optimized VIVA predictions. A single hydrodynamic database is used. In this figure we represent the change in spanwise RMS response as the training is performed in the 3 catenary plane orientations to which this specific case does not belong to, in this particular case $\phi = 0°, 60°, 90°$. For the relation between experiment labels and catenary plane orientations & towing velocities Table 1 can be consulted. (For interpretation of the references to color in this figure legend, the reader is referred to the web version of this article.)

of a tangential component of water velocity relative to the SCR riser at this orientation, constituting a worst-case scenario for current drag on the SCR riser and causing significant deviations from the hydrostatic shape. Such deviations imply that the assumptions made in Section 3 may not hold, potentially compromising the prediction capabilities of our VIV model. Moreover, VIV may evolve into a wide-band response due to strong variability in added mass and wake capture phenomena (Williamson and Govardhan, 2004; Morse and Williamson, 2009; Modarres-Sadeghi et al., 2011), further affecting prediction accuracy.

Overall, the obtained optimized databases that perform best after random initializations, can be described as having characteristic C_{lv} contours that predict more accurate and overall smaller VIV amplitudes than when using databases extracted from rigid cylinders. To clearly observe this compare Figs. 7 to 8, this last one leans on the conservative side of predictions to be able to ensure that risers vibrations are not underpredicted for a wide range of situations.

In our study, we also undertake a comprehensive comparison with predictions derived from databases based on rigid cylinder experiments. These databases have historically been a standard reference in the field, primarily due to their conservative nature in predicting Vortex-Induced Vibrations (VIV) amplitudes. It is important to understand that these traditional databases, while reliable, often provide overestimated predictions, leading to more conservative designs and assessments in marine engineering applications. By contrasting our optimized databases against these established models, we aim to highlight not only the differences in predictive accuracy but also the potential for more refined and less conservative designs. This comparative analysis allows us to demonstrate the efficacy of our approach in yielding more precise predictions, thereby offering a pathway towards optimizing design parameters in the marine engineering sector. The critical insight gained from this comparison is instrumental in advancing our understanding of hydrodynamic forces and their impact on offshore structures, leading to a more nuanced and effective approach to design and safety assessments.

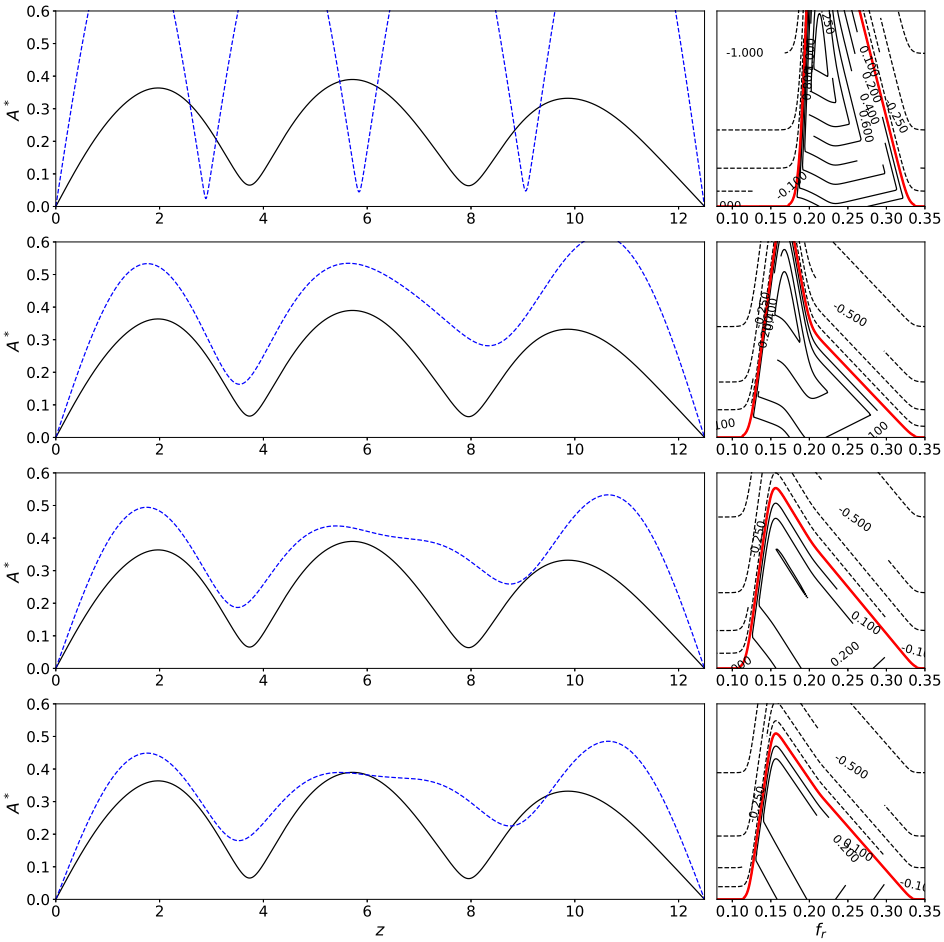

Fig. 4. Test case 3000. *Cross flow RMS predictions, testing catenary plane angle with velocity* $\phi = 60°$. Solid black curve are reconstructed displacements and blue-dashed line are optimized VIVA predictions. A single hydrodynamic database is used. In this figure we represent the change in spanwise RMS response as the training is performed in the 3 catenary plane orientations to which this specific case does not belong to, in this particular case $\phi = 0°, 30°, 90°$. For the relation between experiment labels and catenary plane orientations & towing velocities Table 1 can be consulted. (For interpretation of the references to color in this figure legend, the reader is referred to the web version of this article.)

6. Conclusion

The methodology is successfully cross-validated considering four different current incidence angles, performed with the objective of evaluating the generalization properties of the learned hydrodynamic databases. By systematically leaving out the training data of the experiments pertaining to one of these current directions, we evaluate the effect on the statistics of the riser dynamics learned in the hydrodynamic databases. Furthermore we evaluate the extrapolation capabilities of the methodology when using the databases learned when $\phi = 0, 90°$ are not included in the training data.

The exercise previously described successfully shows good performance of the prediction capabilities of the databases extracted, indicated by the strong positive correlation between training and testing errors shown in Figs. D.15 and D.16. Furthermore, to provide a better intuition of how the learning generalizes in testing phase, the evolution of the prediction of spanwise RMS of the CF Amplitudes is provided in Figs. 2 to 5. In this figures it can clearly be seen how the learned hydrodynamic databases converge to correctly predict the predominant modes and amplitude of VIV dynamics.

The novel contribution we put forward in this systematic study is the extension of the method (Rudy et al., 2021) performed to show generalization properties of hydrodynamic databases. The specific model used to predict VIV (Zheng et al., 2011a) is secondary to the data assimilation process, since hydrodynamic data bases are not limited to this model and we just want to highlight the potential that they have to improve VIV prediction methods from field measurements, in a way that is easy to interpret and extract physical insights. One example where such hydrodynamic databases may be applied are wake oscillator models (Ma and Srinil, 2023) to mitigate absent physics (Modarres-Sadeghi, 2022), consequence of not modeling the prohibitively costly Navier–Stokes equations. Moreover, we expect that as the VIV prediction tools improve while using the methodology that we put forward in this paper, the complexity and extension of existing hydrodynamic databases will increase. Enabling a more complex behavior characterization, that currently is mostly based on the VIV observed in rigid cylinders (Zheng et al., 2011b, 2014).

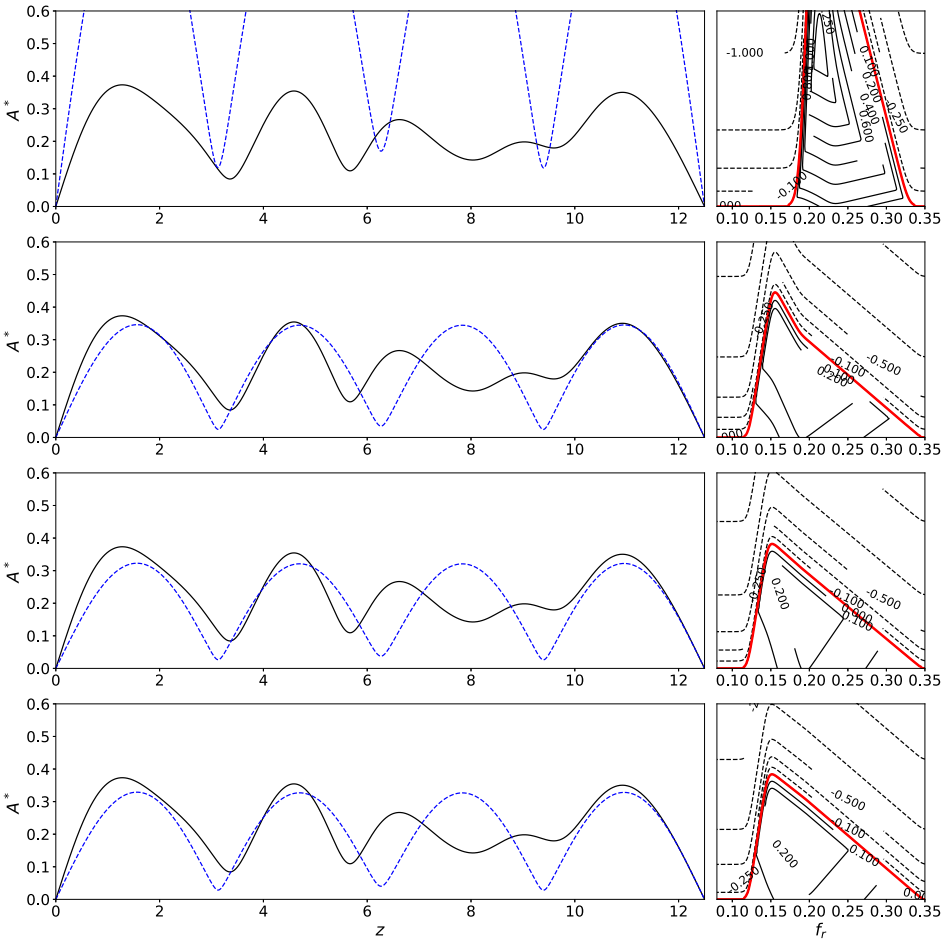

Fig. 5. Test case 4000. *Cross flow RMS predictions, testing catenary plane angle with velocity* $\phi = 90°$. Solid black curve are reconstructed displacements and blue-dashed line are optimized VIVA predictions. A single hydrodynamic database is used. In this figure we represent the change in spanwise RMS response as the training is performed in the 3 catenary plane orientations to which this specific case does not belong to, in this particular case $\phi = 0°, 30°, 60°$. For the relation between experiment labels and catenary plane orientations & towing velocities Table 1 can be consulted. (For interpretation of the references to color in this figure legend, the reader is referred to the web version of this article.)

CRediT authorship contribution statement

José del Águila Ferrandis: Data curation, Investigation, Methodology, Writing – original draft, Writing – review & editing. **Andreas Mentzelopoulos:** Formal analysis, Methodology, Validation. **Edvard Ronglan:** Data curation, Investigation, Methodology, Project administration. **Samuel Rudy:** Investigation, Methodology, Supervision, Validation. **Dixia Fan:** Conceptualization, Data curation, Supervision. **Themistoklis Sapsis:** Conceptualization, Supervision. **Michael S. Triantafyllou:** Conceptualization, Supervision, Writing – original draft, Writing – review & editing.

Declaration of competing interest

The authors declare that they have no known competing financial interests or personal relationships that could have appeared to influence the work reported in this paper.

Data availability

Data will be made available on request.

Acknowledgment

We would just like to acknowledge the support of the Digimar Consortium.

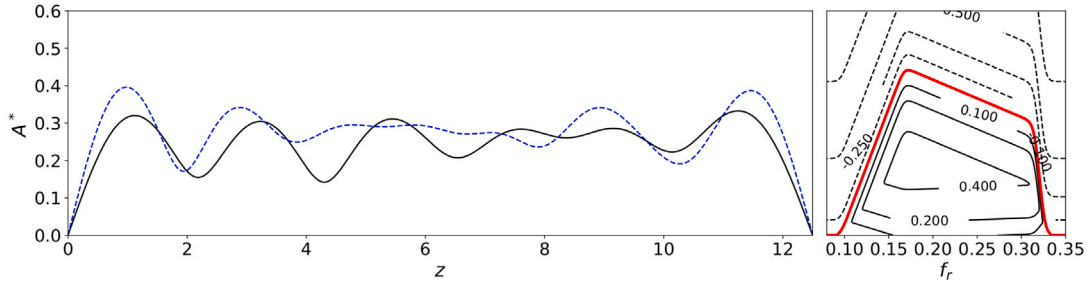

(a) Experiment 1022 at 0.34 m/s and Direction 0°.

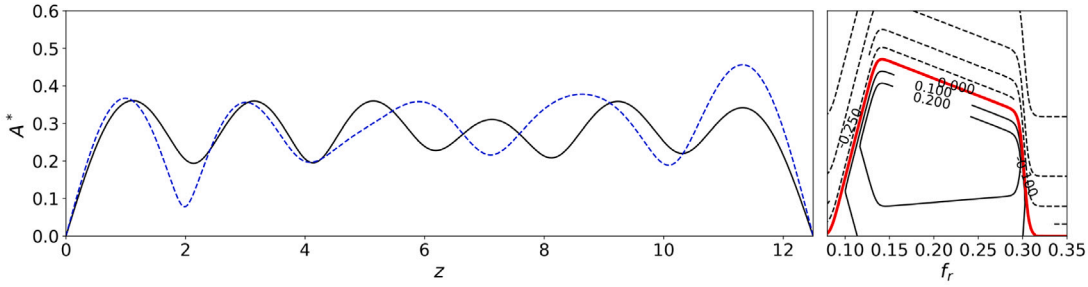

(b) Experiment 2022 at 0.34 m/s and Direction 30°.

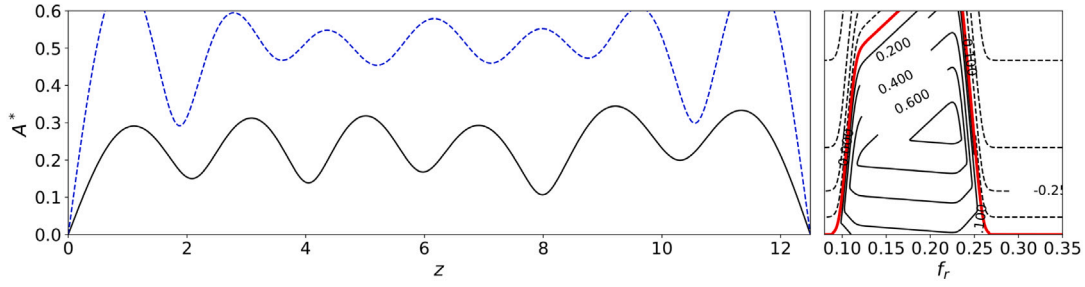

(c) Experiment 3022 at 0.34 m/s and Direction 60°.

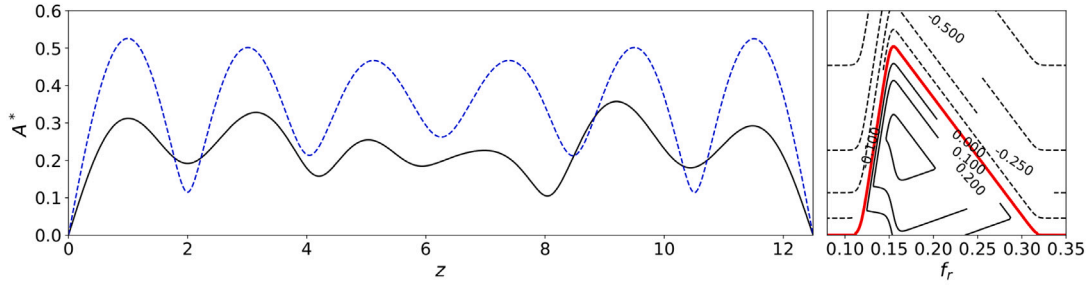

(d) Experiment 4022 at 0.34 m/s and Direction 90°.

Fig. 6. Comparative Analysis of Experiments at a Uniform Current Velocity of 0.34 m/s. This figure showcases the results from experiments 1022, 2022, 3022, and 4022, each conducted at the same current velocity but varying current directions: 0°, 30°, 60°, and 90°, respectively. The juxtaposition of these experiments highlights the influence of current direction on hydrodynamic responses.

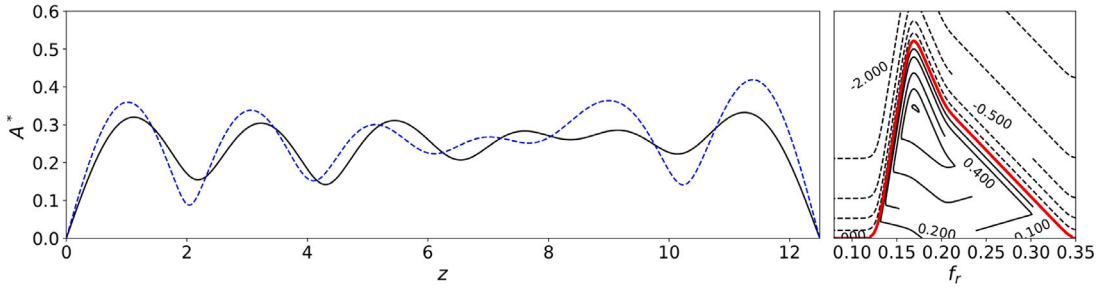

(a) Experiment 1022 at 0.34 m/s and Direction 0°.

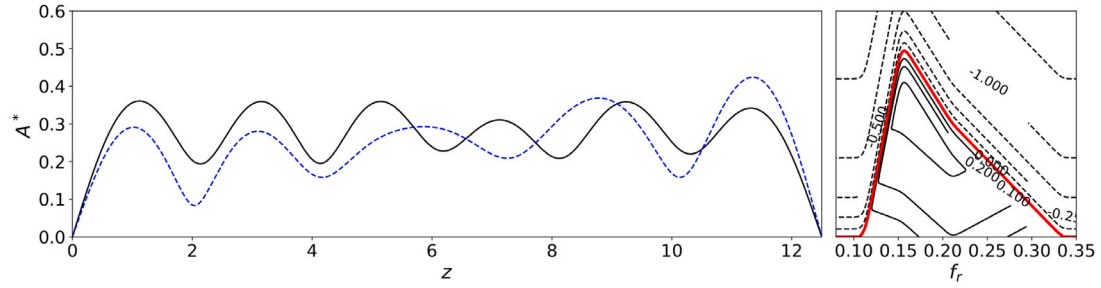

(b) Experiment 2022 at 0.34 m/s and Direction 30°.

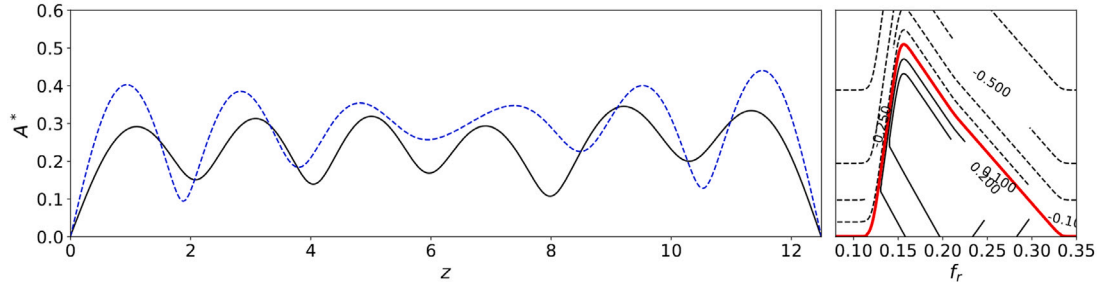

(c) Experiment 3022 at 0.34 m/s and Direction 60°.

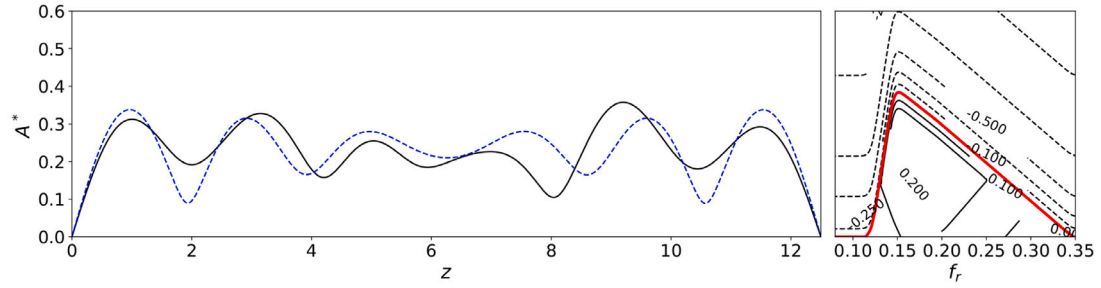

(d) Experiment 4022 at 0.34 m/s and Direction 90°.

Fig. 7. Enhanced Optimization with Parameter Constraints in Hydrodynamic Database Training. Displayed are results from experiments 1022, 2022, 3022, and 4022, each at a uniform current velocity of 0.34 m/s but different current directions (0°, 30°, 60°, and 90°). For these experiments, parameter constraints were applied during training whenever existing experimental data were available. This approach facilitates easier optimization problems and better generalization, resulting in more consistent hydrodynamic databases when learning from diverse sets of angles.

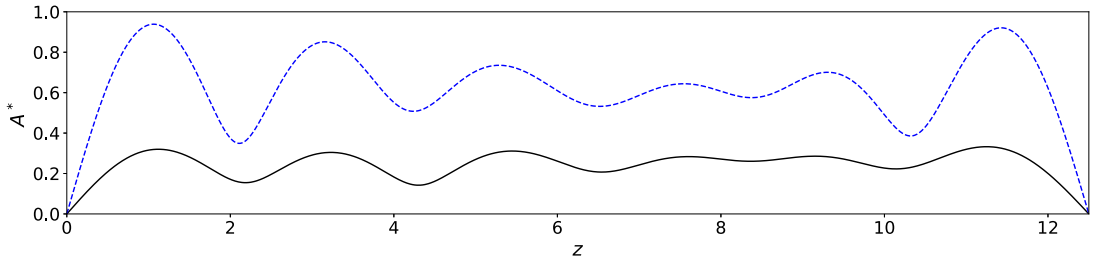

(a) Experiment 1022 at 0.34 m/s and Direction 0°.

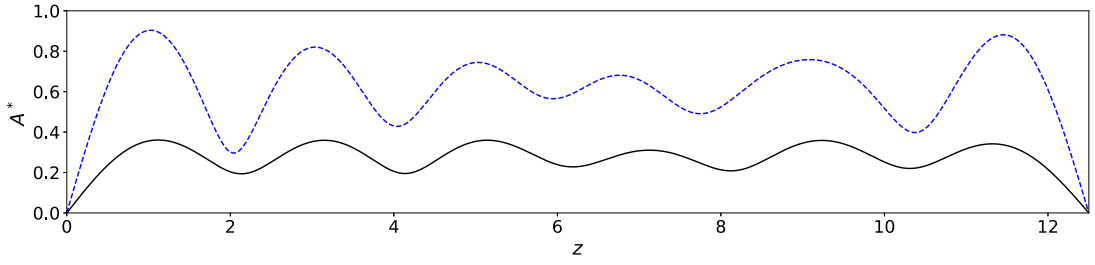

(b) Experiment 2022 at 0.34 m/s and Direction 30°.

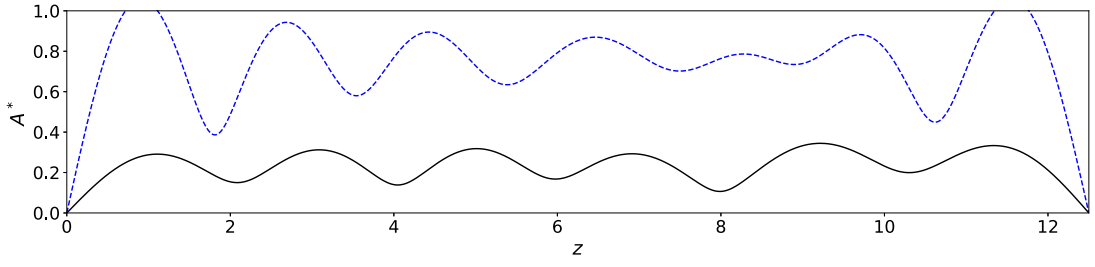

(c) Experiment 3022 at 0.34 m/s and Direction 60°.

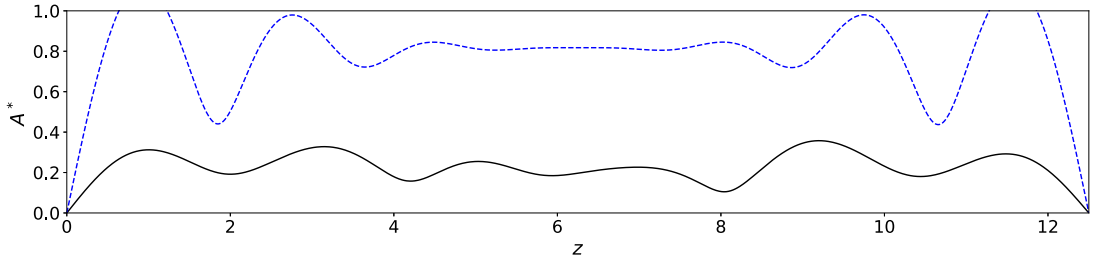

(d) Experiment 4022 at 0.34 m/s and Direction 90°.

Fig. 8. Predictions provided by standard VIVA database. Displayed are results from experiments 1022, 2022, 3022, and 4022, each at a uniform current velocity of 0.34 m/s but different current directions (0°, 30°, 60°, and 90°). For these experiments, parameter constraints were applied during training whenever existing experimental data were available. This approach facilitates easier optimization problems and better generalization, resulting in more consistent hydrodynamic databases when learning from diverse sets of angles.

Appendix A. Norwegian Deepwater Programme (NDP) experimental overview and riser motion reconstruction

Experimental data from the Norwegian Deepwater Programme (NDP) (Braaten and Lie, 2005) has been used to test the optimization algorithms presented in this paper. The experiments were performed by NDP in the MARINTEK Offshore Basin on a steel catenary riser (SCR) with high length-to-diameter ratio (L/D) risers. The experimental data was collected by accelerometer sensors along the riser, in both the In-Line (IL) and Cross-FLow (CF) directions. The SCR riser, used in these experiments has length

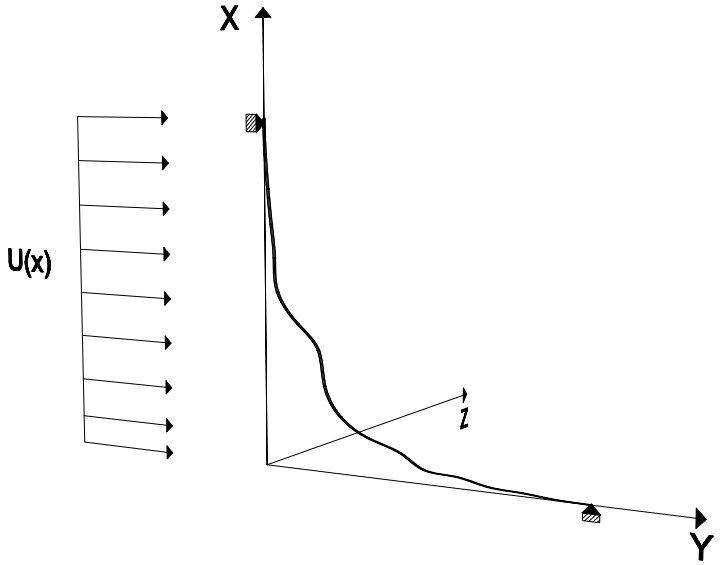

Fig. A.9. Flexible SCR riser within a uniform flow profile.

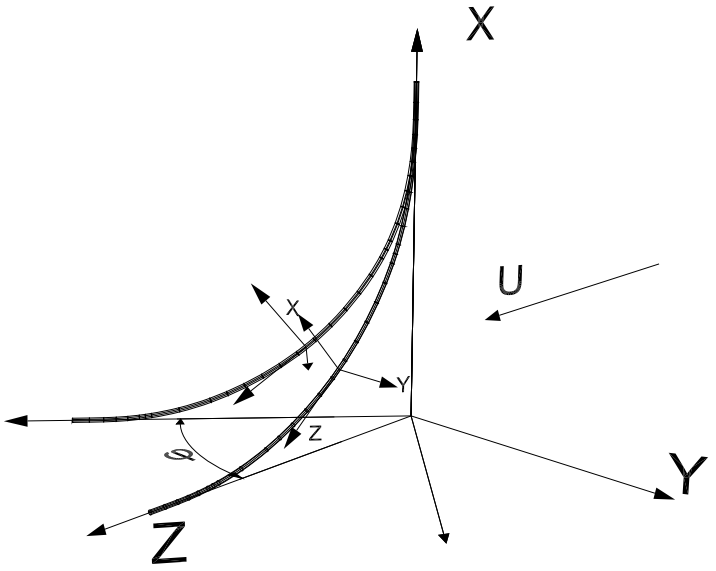

Fig. A.10. Reference frame used to reconstruct riser deformed shape from sensor readings. The angle with respect to the flow is controlled by ϕ.

$L_{Riser} = 12.5$ m and outer diameter $D_{Riser} = 14$ mm. The number of transducers recording accelerations do not vary in the IL and CF directions (see Fig. A.11):

Type	Cross-flow	In-line
Accelerations	10	10

An example case used to benchmark the algorithms we put forward in this publication is characterized by a $0\ deg$ angle between the catenary plane and the flow velocity, which is of 0.12 m/s. There is one single structural mode in the vibration, the 3rd mode both in CF and IL vibrations, as one can see in Fig. A.12 & Fig. A.13. Moreover, inspecting time animations of the deformed shape it is easy to see that there are no traveling waves (see Fig. A.9).

A complex post-processing framework is adopted to calculate the time-varying deformed shape of the riser, which we describe herein. The difficulty in reconstructing the deformed shape is that we rely on a number of strain and acceleration measurements at discrete points along the riser (Mukundan, 2008). Here we describe the formulation only for CF displacements, because IL

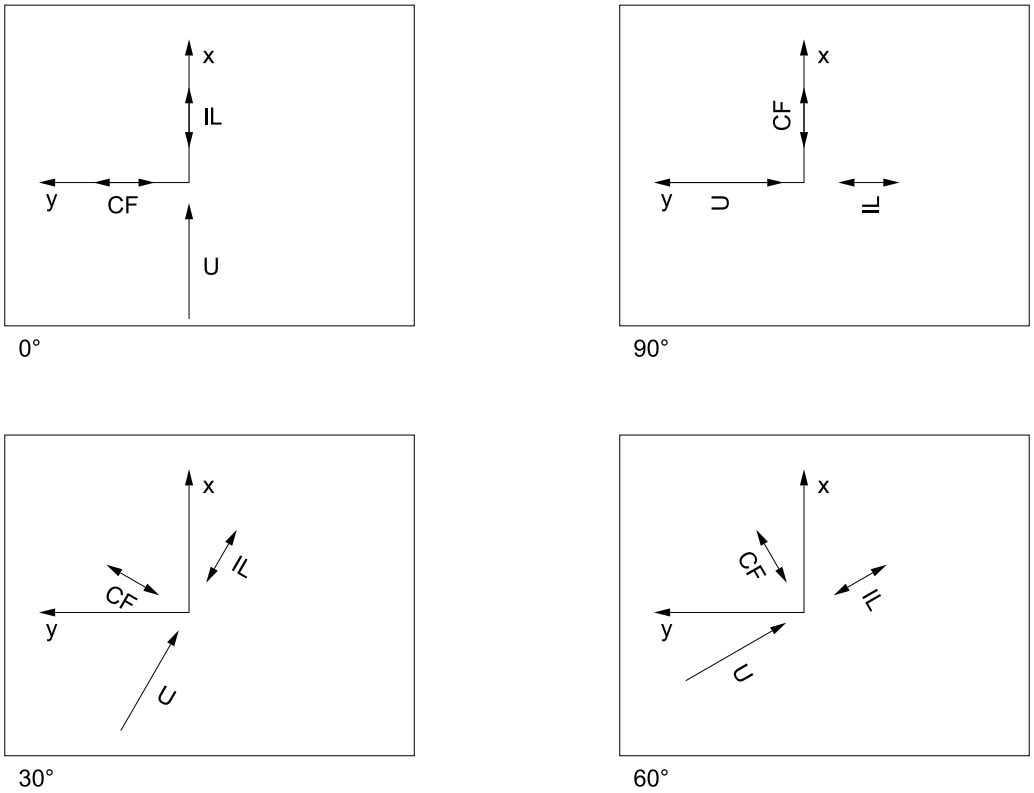

Fig. A.11. The definitions of cross-flow and in-line vibration directions for the riser are adapted for each of the four catenary plane orientations. This adjustment is necessary because the orientation of the sensors and their channels varies when the riser is rotated to test different catenary plane orientations.

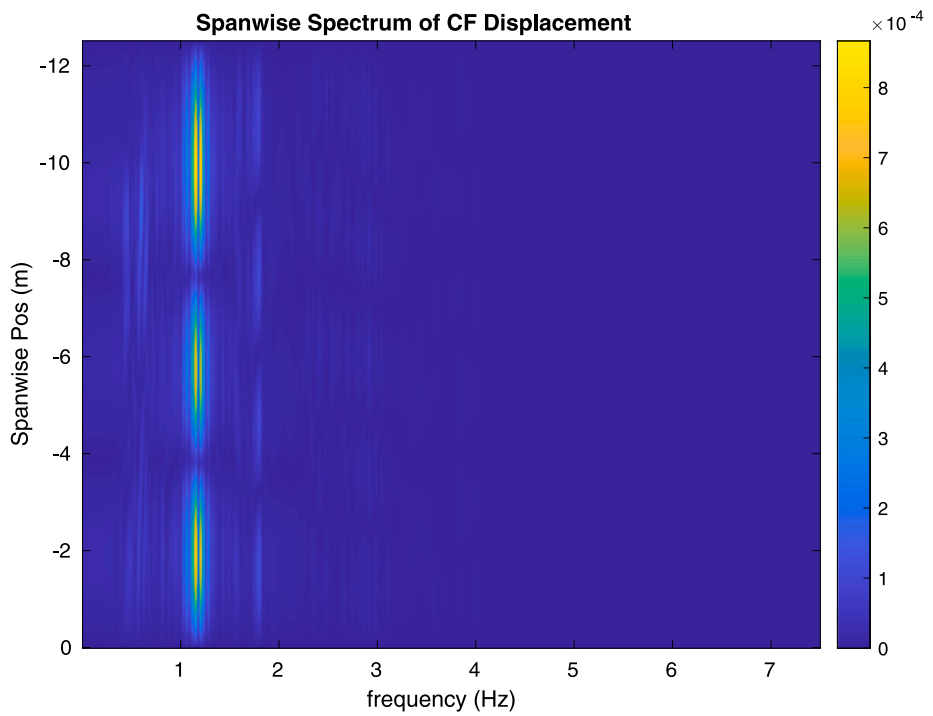

Fig. A.12. Spanwise spectrum of cross-flow displacements.

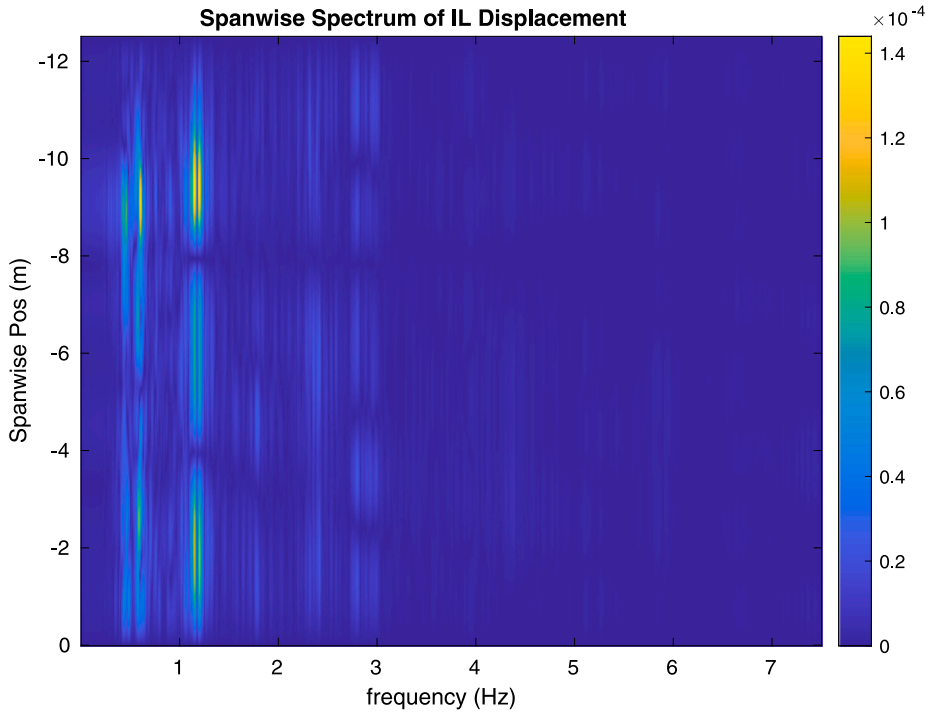

Fig. A.13. Spanwise spectrum of in-line displacements.

displacements were treated in the same manner. Given that the ends of the riser are fixed, we can use the following Fourier expansion to represent the deformed shape.

$$y(z,t) = \sum_{n=0}^{\infty} w_n(t)\varphi_n(z) \tag{A.1}$$

$$\varphi_n(z) = \sin(n\pi z/L) \tag{A.2}$$

Truncating at an appropriate number of modes N:

$$a(z,t) = \sum_{n=1}^{N} w_{n_{tt}}(t)\varphi_n(z) \tag{A.3}$$

$$\varphi_n(z) = \sin(n\pi z/L) \Rightarrow \varphi''(z) = -(n\pi/L)^2 \sin(n\pi z/L) \tag{A.4}$$

We exploit the fact that the measurements are sampled at high frequency in time by using the following Fourier transforms:

$$\mathcal{F}\{w_n(t)\} = \hat{w}_n(\omega) \tag{A.5}$$

$$\mathcal{F}\{y(z,t)\} = \hat{y}(z,\omega) \tag{A.6}$$

$$\mathcal{F}\{a(z,t)\} = \hat{a}(z,\omega) \tag{A.7}$$

From which we can obtain:

$$\hat{y}(z,\omega) = \sum_{n=1}^{N} \hat{w}_n(\omega)\phi_n(z) \tag{A.8}$$

$$\hat{a}(z,\omega) = -\omega^2 \hat{y}(z,\omega) = -\omega^2 \sum_{n=1}^{N} \hat{w}_n(\omega)\phi_n(z) \tag{A.9}$$

Expressing the problem in the frequency domain allows expressing the previous three equations in matrix form as shown below:

$$\boldsymbol{\Phi}\hat{\boldsymbol{W}} = \hat{\boldsymbol{Y}}, \tag{A.10}$$

where,

$$\hat{W} = \begin{bmatrix} \imath\hat{w}_1(\omega_1) & \imath\hat{w}_1(\omega_2) & \dots & \imath\hat{w}_1(\omega_\Lambda) \\ \imath\hat{w}_2(\omega_1) & \imath\hat{w}_2(\omega_2) & \dots & \imath\hat{w}_2(\omega_\Lambda) \\ \imath\hat{w}_3(\omega_1) & \imath\hat{w}_3(\omega_2) & \dots & \imath\hat{w}_3(\omega_\Lambda) \\ \vdots & \vdots & \ddots & \vdots \\ \imath\hat{w}_N(\omega_1) & \imath\hat{w}_N(\omega_2) & \dots & \imath\hat{w}_N(\omega_\Lambda) \end{bmatrix}, \tag{A.11}$$

$$\boldsymbol{\Phi} = \begin{bmatrix} \boldsymbol{\Phi}_1(z_1) & \boldsymbol{\Phi}_2(z_1) & \dots & \boldsymbol{\Phi}_N(z_1) \\ \boldsymbol{\Phi}_1(z_2) & \boldsymbol{\Phi}_2(z_2) & \dots & \boldsymbol{\Phi}_N(z_2) \\ \boldsymbol{\Phi}_1(z_3) & \boldsymbol{\Phi}_2(z_3) & \dots & \boldsymbol{\Phi}_N(z_3) \\ \vdots & \vdots & \ddots & \vdots \\ \boldsymbol{\Phi}_1(z_{M_y}) & \boldsymbol{\Phi}_2(z_{M_y}) & \dots & \boldsymbol{\Phi}_N(z_{M_y}) \\ \boldsymbol{\Phi}_1(z_1) & \boldsymbol{\Phi}_2(z_1) & \dots & \boldsymbol{\Phi}_N(z_1) \\ \boldsymbol{\Phi}_1(z_2) & \boldsymbol{\Phi}_2(z_2) & \dots & \boldsymbol{\Phi}_N(z_2) \\ \boldsymbol{\Phi}_1(z_3) & \boldsymbol{\Phi}_2(z_3) & \dots & \boldsymbol{\Phi}_N(z_3) \\ \vdots & \vdots & \ddots & \vdots \\ \boldsymbol{\Phi}_1(z_{M_a}) & \boldsymbol{\Phi}_2(z_{M_a}) & \dots & \boldsymbol{\Phi}_N(z_{M_a}) \end{bmatrix}, \tag{A.12}$$

$$\hat{Y} = \begin{bmatrix} \hat{y}(z_1,\omega_1) & \hat{y}(z_1,\omega_2) & \dots & \hat{y}(z_1,\omega_\Lambda) \\ \hat{y}(z_2,\omega_1) & \hat{y}(z_2,\omega_2) & \cdots & \hat{y}(z_2,\omega_\Lambda) \\ \hat{y}(z_3,\omega_1) & \hat{y}(z_3,\omega_2) & \cdots & \hat{y}(z_3,\omega_\Lambda) \\ \vdots & \vdots & \ddots & \vdots \\ \hat{y}(z_{M_y},\omega_1) & \hat{y}(z_{M_y},\omega_2) & \cdots & \hat{y}(z_{M_y},\omega_\Lambda) \\ \frac{-\hat{a}(z_1,\omega_1)}{\omega_1^2} & \frac{-\hat{a}(z_1,\omega_2)}{\omega_2^2} & \dots & \frac{-\hat{a}(z_1,\omega_\Lambda)}{\omega_\Lambda^2} \\ \frac{-\hat{a}(z_2,\omega_1)}{\omega_1^2} & \frac{-\hat{a}(z_2,\omega_2)}{\omega_2^2} & \dots & \frac{-\hat{a}(z_2,\omega_\Lambda)}{\omega_\Lambda^2} \\ \frac{-\hat{a}(z_3,\omega_1)}{\omega_1^2} & \frac{-\hat{a}(z_3,\omega_2)}{\omega_2^2} & \dots & \frac{-\hat{a}(z_3,\omega_\Lambda)}{\omega_\Lambda^2} \\ \vdots & \vdots & \ddots & \vdots \\ \frac{-\hat{a}(z_{M_a},\omega_1)}{\omega_1^2} & \frac{-\hat{a}(z_{M_a},\omega_2)}{\omega_2^2} & \dots & \frac{-\hat{a}(z_{M_a},\omega_\Lambda)}{\omega_\Lambda^2} \end{bmatrix}. \tag{A.13}$$

We solve for each value of ω using the pseudo-inverse $\boldsymbol{\Phi}^+$.

$$\imath\hat{w} = \boldsymbol{\Phi}^+\hat{Y} \tag{A.14}$$

Taking a inverse Fourier transform of $\imath\hat{w}$, we find the coefficient matrix in the time domain, and the riser CF displacement is found:

$$y(z,t) = \sum_{n=0}^{N} w_n(t)\varphi_n(z) \tag{A.15}$$

Finding high order modes in Eq. (A.10) requires a minimum number of sensors. Furthermore the use of the pseudo-inverse $\boldsymbol{\Phi}^+$ is equivalent to a least-squares fit in the frequency domain. Therefore the number of sensors available will limit the number of modes N we can use.

To improve the quality of reconstruction, we employed band-pass filtering to remove low and high frequency noise. used different weighting for the strain and acceleration measurements.

Appendix B. Description of parametric forms for C_{lv} and C_{my}

See Fig. B.14.

Appendix C. Single peak parametrization for hydrodynamic databases

This appendix provides a detailed overview of the single peak parametrization, which is one of the two parametrizations developed for hydrodynamic databases, particularly valuable in marine engineering fluid dynamics. This parametrization consists of fourteen parameters, each designed to capture specific hydrodynamic characteristics. The descriptions and functionalities of these parameters are listed in Table C.2.

The conceptual foundation of this parametrization is inspired by earlier studies, such as those using piecewise linear databases (Mukundan, 2008). However, our approach introduces a key modification to enable smoother transitions between the linear segments of the model. This is achieved through the implementation of the soft-plus function, given by:

$$s_w(x) = w\,\log(1+\exp(x/w)). \tag{C.1}$$

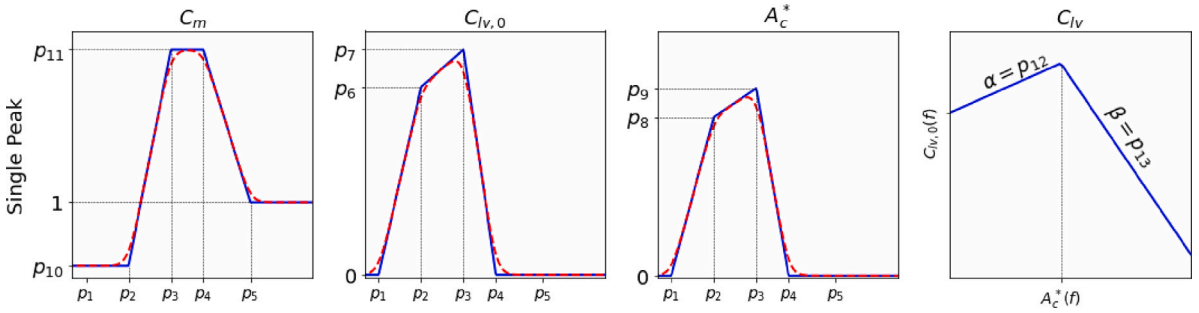

Fig. B.14. Single peak parametrization used for C_{lv} and C_{my}. Blue curve shows piecewise linear parametrization realized when $p_{14} = 0$. Red dashed line is smoothed version from $p_{14} = 0.003$.

Table C.2
Description of parameters for single peak hydrodynamic database.

$p_1 - p_5$	Reduced frequencies used for C_m, $C_{lv,0}$, and A_c^*.
p_6, p_7	Parameters for values of $C_{lv,0}$ at p_2, p_3.
p_8, p_9	Parameters for values of A_c^* at p_2, p_3.
p_{10}, p_{11}	Values of constant sections of C_m curve.
p_{12}	Increasing slope of C_{lv} w.r.t. A^* for $A^* < A_c^*$
p_{13}	Decreasing slope of C_{lv} w.r.t. A^* for $A^* > A_c^*$

Table C.3
Description and bounds of parameters for hydrodynamic coefficients in single peak parametrization.

p_1	$(0.08, 0.35)$	p_6	$(0, 0.5)$	p_{11}	$(1, 10)$
p_2	$(p_1, 0.35)$	p_7	$(0, 0.5)$	p_{12}	$(0.1, 5)$
p_3	$(p_2, 0.35)$	p_8	$(0, 2)$	p_{13}	$(1, 5)$
p_4	$(p_3, 0.35)$	p_9	$(0, 2)$	p_{14}	$(10^{-5}, 0.005)$
p_5	$(p_4, 0.35)$	p_{10}	$(-2, 1)$		

In this formulation, the parameter w is crucial as it determines the length-scale over which the function transitions. This allows for a gradual and smooth change from a value near zero (for $x < 0$) to approximately x (for $x > 0$). The integration of the soft-plus function into the parametrization helps in achieving a more nuanced and flexible modeling approach, compared to the conventional piecewise linear methods. This enhancement is particularly beneficial for accurately capturing the complex behaviors in hydrodynamic scenarios.

The added mass term, C_{my}, in the context of the single peak parametrization, is a univariate function of reduced frequency. This model divides C_{my} into three distinct regions, each characterized by constant values separated by linear transitions that are smoothed at the corners. For clarity, examples of the single peak variant of C_m are depicted in the leftmost column of Fig. B.14.

Similarly, the lift coefficient, C_{lv}, is formulated as a piecewise linear function of the amplitude A^*. It features a zero-intercept at $C_{lv,0}$ and a critical amplitude A_c^*, which marks the transition point in the coefficient's behavior. These characteristics are modeled as smoothed piecewise linear functions of the reduced frequency f_r. Illustrations of $C_{lv,0}$, A_c^*, and C_{lv} under the single peak parametrization are shown in the subsequent columns of Fig. B.14, specifically highlighted in the top row of the figure.

The following subsection provides a detailed computation and explanation of each parameter and function within the single peak parametrization, as exemplified in Fig. B.14.

C.1. Single peak parametrization

We will use the standard notation s_w to denote the soft-plus function with learned characteristic width $w = p_{14}$ The added mass coefficient is given by,

$$C_m = p_{10} + m_1(s_w(f - p_2) - s_w(f - p_3)) + m_2(s_w(f - p_4) - s_w(f - p_5)) \tag{C.2}$$

where,

$$m_1 = \frac{p_{11} - p_{10}}{p_3 - p_2} \quad \text{and} \quad m_2 = \frac{1 - p_{11}}{p_5 - p_4}. \tag{C.3}$$

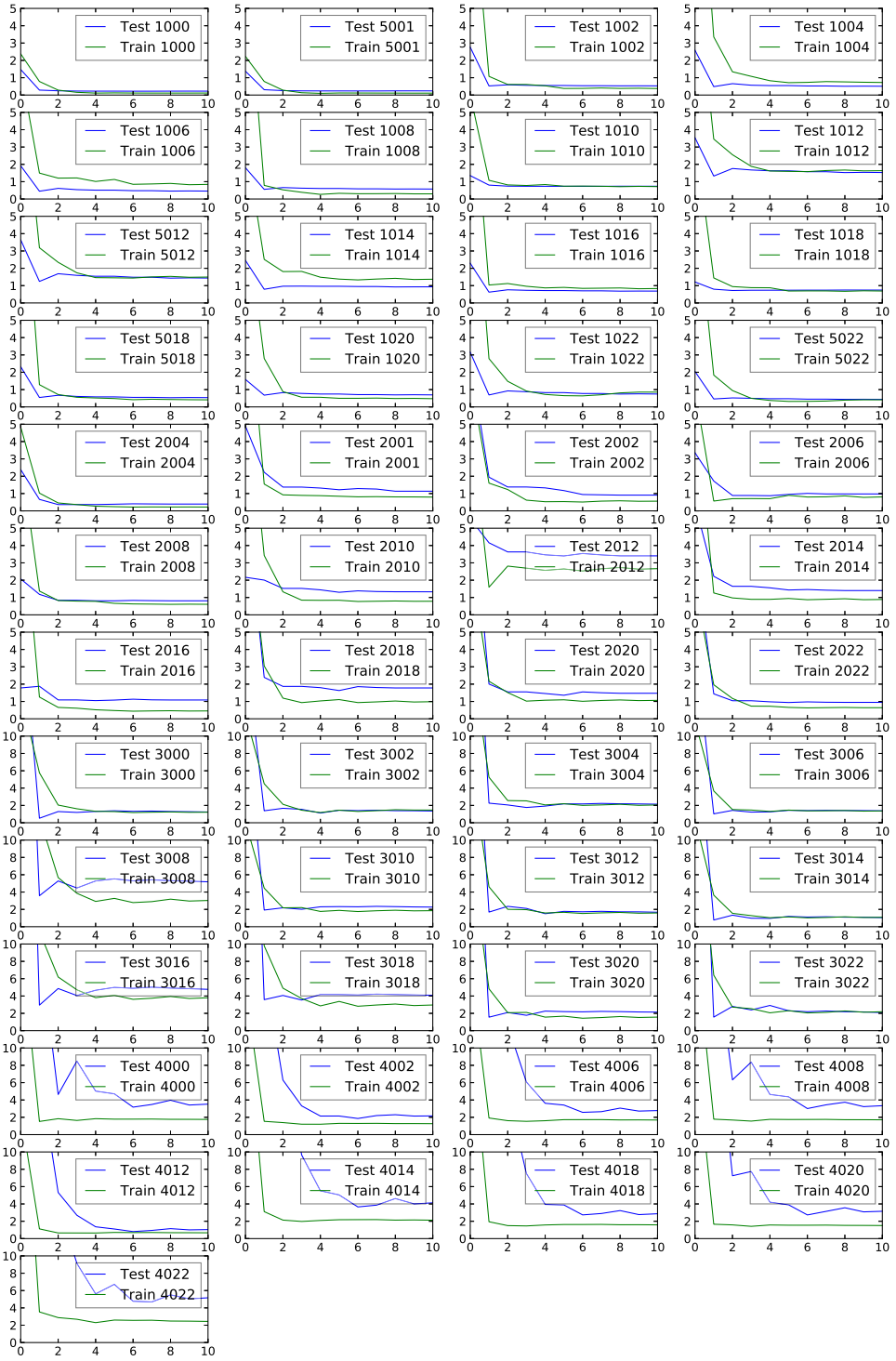

Fig. D.15. Test and train *amplitude* RSE Learning Curves. The vertical axis denotes vibration amplitude (adimensionalized) RSE, and the horizontal axis tracks model evaluation over a fixed number of optimization steps. For any one plot the *test learning curve* represents the loss function when the experiment is left out of the training. This is when its current direction is left out of the training process in the cross-validation. On the other hand, the *train learning curve* is the average of the 3 scenarios when its current direction is part of the training process. Decreasing error on both the training and testing curves suggests a positive correlation between the model's ability to learn from known data and generalize to new situations. As the model becomes more accurate in interpreting training data, its predictions for unseen data also improve, indicating a consistent and effective learning process. This correlation is key for ensuring the model's reliability and applicability in real-world scenarios. Three out of four times any one case is considered in the training, when performing cross-validation across 4 different catenary plane orientations with the flow. The catenary plane orientation of any case can be consulted in Table 1. (For interpretation of the references to color in this figure legend, the reader is referred to the web version of this article.)

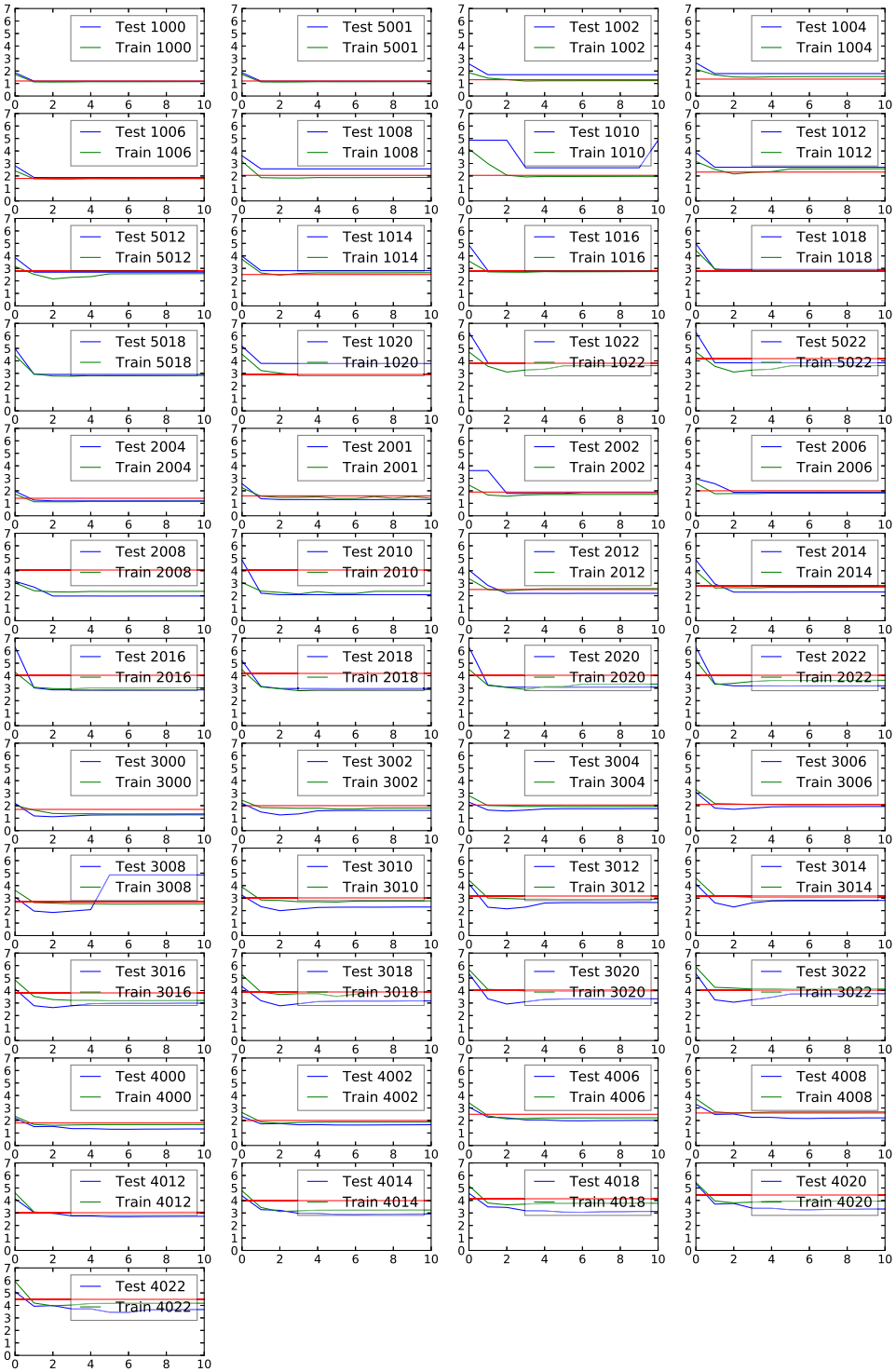

Fig. D.16. Learning Curves for Test and Train Frequency. The vertical axis denotes frequency (Hz), and the horizontal axis tracks model evaluation over a fixed number of optimization steps. The 'Test Learning Curve' represents the loss function when an experiment's current direction is omitted from the training during cross-validation. Conversely, the 'Train Learning Curve' averages outcomes from the three scenarios where the current direction is included in training. Decreasing error on both the training and testing curves suggests a positive correlation between the model's ability to learn from known data and generalize to new situations. As the model becomes more accurate in interpreting training data, its predictions for unseen data also improve, indicating a consistent and effective learning process. This correlation is key for ensuring the model's reliability and applicability in real-world scenarios. This process, applied across four different catenary plane orientations relative to the flow, implies each case is trained three out of four times and considered for testing one time. Refer to Table 1 for details on catenary plane orientations. (For interpretation of the references to color in this figure legend, the reader is referred to the web version of this article.)

The values of $C_{lv,0}$ and A_c^* are given by,

$$C_{lv,0} = m_3(s_w(f-p_1) - s_w(f-p_2)) + m_4(s_w(f-p_2) - s_w(f-p_3)) + m_5(s_w(f-p_3) - s_w(f-p_4)) \tag{C.4}$$

and

$$A_c^* = m_6(s_w(f-p_1) - s_w(f-p_2)) + m_7(s_w(f-p_2) - s_w(f-p_3)) + m_8(s_w(f-p_3) - s_w(f-p_4)), \tag{C.5}$$

where

$$\begin{aligned} m_3 &= \frac{p_6}{p_2-p_1} & m_6 &= \frac{p_8}{p_2-p_1} \\ m_4 &= \frac{p_7-p_6}{p_3-p_2} & m_7 &= \frac{p_9-p_8}{p_3-p_2} \\ m_5 &= \frac{-p_7}{p_4-p_3} & m_8 &= \frac{-p_9}{p_4-p_3} \end{aligned} \tag{C.6}$$

The lift coefficient is given by,

$$C_{lv} = \begin{cases} C_{lv,0} + A^* p_{12}, & \text{if } A^* \le A_c^* \\ C_{lv,0} + A_c^* p_{12} - (A^* - A_c^*)p_{13}, & \text{if } A^* > A_c^* \end{cases} \tag{C.7}$$

Each variable is bounded based on the intervals described in Table C.3. Open boundaries are enforced through fitting the transformed variables $q_i = \sigma^{-1}((p_i - p_{min})/(p_{max} - p_{min}))$ where p_{min} and p_{max} are the bounds for the given parameter and σ is the sigmoid function, which smoothly transforms $\mathbb{R}$ into $(0, 1)$.

Appendix D. Optimized databases convergence study

See Figs. D.15 and D.16.

References

Baarholm, G., Larsen, C., Lie, H., 2006. On fatigue damage accumulation from in-line and cross-flow vortex-induced vibrations on risers. J. Fluids Struct. 22 (1), 109–127. http://dx.doi.org/10.1016/j.jfluidstructs.2005.07.013, URL https://www.sciencedirect.com/science/article/pii/S0889974605001234.

Bearman, P.W., 1984. Vortex shedding from oscillating bluff bodies. Annu. Rev. Fluid Mech. 16 (1), 195–222. http://dx.doi.org/10.1146/annurev.fl.16.010184.001211.

Bourguet, R., Karniadakis, G.E., Triantafyllou, M.S., 2011. Vortex-induced vibrations of a long flexible cylinder in shear flow. J. Fluid Mech. 677, 342–382. http://dx.doi.org/10.1017/jfm.2011.90.

Bourguet, R., Karniadakis, G.E., Triantafyllou, M.S., 2013. Distributed lock-in drives broadband vortex-induced vibrations of a long flexible cylinder in shear flow. J. Fluid Mech. 717, 361–375. http://dx.doi.org/10.1017/jfm.2012.576.

Bourguet, R., Lucor, D., Triantafyllou, M.S., 2012. Mono- and multi-frequency vortex-induced vibrations of a long tensioned beam in shear flow. J. Fluids Struct. 32, 52–64. http://dx.doi.org/10.1016/j.jfluidstructs.2011.05.008, The 7th International Symposium on Fluid-Structure Interactions, Flow-Sound Interactions, and Flow-Induced Vibrations & Noise.

Braaten, H., Lie, H., 2004. NDP Riser High Mode VIV Tests. Technical Report, (512394.00), Norwegian Marine Technology Research Institute, p. 01.

Braaten, H., Lie, H., 2005. NDP riser high mode VIV tests main report. In: MARINTEK report. Trondheim, Norway.

Chaplin, J., Bearman, P., Huera Huarte, F., Pattenden, R., 2005. Laboratory measurements of vortex-induced vibrations of a vertical tension riser in a stepped current. J. Fluids Struct. 21 (1), 3–24. http://dx.doi.org/10.1016/j.jfluidstructs.2005.04.010, Fluid-Structure and Flow-Acoustic Interactions involving Bluff Bodies, URL https://www.sciencedirect.com/science/article/pii/S0889974605001465.

Chaplin, J., King, R., 2018. Laboratory measurements of the vortex-induced vibrations of an untensioned catenary riser with high curvature. J. Fluids Struct. 79, 26–38. http://dx.doi.org/10.1016/j.jfluidstructs.2018.01.008, URL https://www.sciencedirect.com/science/article/pii/S0889974617300798.

Chatjigeorgiou, I.K., Damy, G., LeBoulluec, M., 2008. Numerical and experimental investigation on the dynamics of catenary risers and the riser-induced-damping phenomenon. In: International Conference on Offshore Mechanics and Arctic Engineering, Vol. 48180. pp. 671–680.

Dahl, J.M., Hover, F.S., Triantafyllou, M.S., Oakley, O.H., 2010. Dual resonance in vortex-induced vibrations at subcritical and supercritical Reynolds numbers. J. Fluid Mech. 643, 395–424. http://dx.doi.org/10.1017/S0022112009992060.

Evangelinos, C., Karniadakis, G.E., 1999. Dynamics and flow structures in the turbulent wake of rigid and flexible cylinders subject to vortex-induced vibrations. J. Fluid Mech. 400, 91–124.

Facchinetti, M., de Langre, E., Biolley, F., 2004. Coupling of structure and wake oscillators in vortex-induced vibrations. J. Fluids Struct. 19 (2), 123–140. http://dx.doi.org/10.1016/j.jfluidstructs.2003.12.004.

Fan, D., Wang, Z., Triantafyllou, M., et al., 2019. Mapping the properties of the vortex-induced vibrations of flexible cylinders in uniform oncoming flow. J. Fluid Mech. 881, 815–858. http://dx.doi.org/10.1017/jfm.2019.738.

Farshidianfar, A., Zanganeh, H., 2010. A modified wake oscillator model for vortex-induced vibration of circular cylinders for a wide range of mass-damping ratio. J. Fluids Struct. 26 (3), 430–441. http://dx.doi.org/10.1016/j.jfluidstructs.2009.11.005.

Feng, C., 1968. The Measurement of Vortex Induced Effects in Flow Past Stationary and Oscillating Circular and D-Section Cylinders (Ph.D. thesis). University of British Columbia.

Gao, Y., Fu, S., Wang, J., Song, L., Chen, Y., 2015. Experimental study of the effects of surface roughness on the vortex-induced vibration response of a flexible cylinder. Ocean Eng. 103, 40–54. http://dx.doi.org/10.1016/j.oceaneng.2015.04.052.

Gedikli, E.D., Chelidze, D., Dahl, J.M., 2018. Observed mode shape effects on the vortex-induced vibration of bending dominated flexible cylinders simply supported at both ends. J. Fluids Struct. 81, 399–417. http://dx.doi.org/10.1016/j.jfluidstructs.2018.05.010, URL https://www.sciencedirect.com/science/article/pii/S088997461730782X.

Gedikli, E.D., Dahl, J.M., Chelidze, D., 2017. Multivariate analysis of vortex-induced vibrations in a tensioned cylinder reveal nonlinear modal interactions. Procedia Eng. 199, 546–551. http://dx.doi.org/10.1016/j.proeng.2017.09.159, X International Conference on Structural Dynamics, EURODYN 2017. URL https://www.sciencedirect.com/science/article/pii/S1877705817336007.

Hover, F., Triantafyllou, M., 1999. Linear dynamics of curved tensioned elastic beams. J. Sound Vib. 4 (228), 923–930.

Huera-Huarte, F., Bearman, P., 2009. Wake structures and vortex-induced vibrations of a long flexible cylinder—Part 1: Dynamic response. J. Fluids Struct. 25 (6), 969–990. http://dx.doi.org/10.1016/j.jfluidstructs.2009.03.007, URL https://www.sciencedirect.com/science/article/pii/S0889974609000449.

Jain, A., Modarres-Sadeghi, Y., 2013. Vortex-induced vibrations of a flexibly-mounted inclined cylinder. J. Fluids Struct. 43, 28–40. http://dx.doi.org/10.1016/j.jfluidstructs.2013.08.005, URL https://www.sciencedirect.com/science/article/pii/S0889974613001734.

Kim, W.-J., Newlin, J., Haws, J., 2006. Experimental and analytical investigation of soil/SCR interaction under VIV. In: The Sixteenth International Offshore and Polar Engineering Conference. OnePetro.

King, R., 1977. Vortex excited oscillations of Yawed circular cylinders. J. Fluids Eng. 99 (3), 495–501. http://dx.doi.org/10.1115/1.3448825, arXiv:https://asmedigitalcollection.asme.org/fluidsengineering/article-pdf/99/3/495/5899790/495_1.pdf.

Larsen, C.M., Vikestad, K., Yttervik, R., Passano, E., Baarholm, G., 2001. VIVANA Theory Manual. Marintek, Trondheim, Norway.

Lu, C.-L., 1994. Three-Dimensional Flexural and Torsional Mechanics of Low and High Tension Cables. University of Michigan.

Ma, B., Srinil, N., 2023. Prediction model for multidirectional vortex-induced vibrations of catenary riser in convex/concave and perpendicular flows. J. Fluids Struct. 117, 103826.

Miliou, A., De Vecchi, A., Sherwin, S.J., Graham, J.M.R., 2007. Wake dynamics of external flow past a curved circular cylinder with the free stream aligned with the plane of curvature. J. Fluid Mech. 592, 89–115. http://dx.doi.org/10.1017/S0022112007008245.

Modarres-Sadeghi, Y., 2022. Introduction to Fluid-Structure Interactions. Springer Nature.

Modarres-Sadeghi, Y., Chasparis, F., Triantafyllou, M., Tognarelli, M., Beynet, P., 2011. Chaotic response is a generic feature of vortex-induced vibrations of flexible risers. J. Sound Vib. 330 (11), 2565–2579.

Morse, T., Williamson, C., 2009. The effect of Reynolds number on the critical mass phenomenon in vortex-induced vibration. Phys. Fluids 21 (4), 045105.

Mukundan, H., 2008. Vortex-Induced Vibration of Marine Risers: Motion and Force Reconstruction from Field and Experimental Data (Ph.D. thesis). Massachusetts Institute of Technology.

Newman, D.J., Karniadakis, G.E., 1997. A direct numerical simulation study of flow past a freely vibrating cable. J. Fluid Mech. 344, 95–136. http://dx.doi.org/10.1017/S002211209700582X.

Pereira, F., Gonçalves, R., Pesce, C., et al., 2013. A model scale experimental investigation on vortex-self induced vibrations (VSIV) of catenary risers, OMAE2013-10447. In: Proceedings of the ASME 32ndth International Conference on Ocean, Offshore and Arctic Engineering, June. pp. 9–14.

Ramberg, S.E., 1983. The effects of yaw and finite length upon the vortex wakes of stationary and vibrating circular cylinders. J. Fluid Mech. 128, 81–107.

Rudy, S., Fan, D., Ferrandis, J.d.A., Sapsis, T., Triantafyllou, M.S., 2021. Learning optimal parametric hydrodynamic database for vortex-induced crossflow vibration prediction. arXiv preprint arXiv:2104.05887.

Sarpkaya, T., 1979. Vortex-induced oscillations: A selective review. J. Appl. Mech. 46 (2), 241–258. http://dx.doi.org/10.1115/1.3424537.

Song, J.n., Lu, L., Teng, B., Park, H.i., Tang, G.q., Wu, H., 2011. Laboratory tests of vortex-induced vibrations of a long flexible riser pipe subjected to uniform flow. Ocean Eng. 38 (11), 1308–1322. http://dx.doi.org/10.1016/j.oceaneng.2011.05.020.

Triantafyllou, G., 1998. Vortex induced vibrations of long cylindrical structures. In: Summer Meeting ASME. Washington, DC.

Triantafyllou, M., Triantafyllou, G., Tein, Y., et al., 1999. Pragmatic riser VIV analysis. In: Offshore Technology Conference.

Trim, A., Braaten, H., Lie, H., Tognarelli, M., 2005. Experimental investigation of vortex-induced vibration of long marine risers. J. Fluids Struct. 21 (3), 335–361. http://dx.doi.org/10.1016/j.jfluidstructs.2005.07.014, Marine and Aeronautical Fluid-Structure Interactions, URL https://www.sciencedirect.com/science/article/pii/S0889974605001325.

Vandiver, J.K., Li, L., 2005. Shear7 V4. 4 Program Theoretical Manual. Massachusetts Institute of Technology.

Wang, J., Fu, S., Baarholm, R., Wu, J., Larsen, C.M., 2014. Fatigue damage of a steel catenary riser from vortex-induced vibration caused by vessel motions. Mar. Struct. 39, 131–156. http://dx.doi.org/10.1016/j.marstruc.2014.07.002, URL https://www.sciencedirect.com/science/article/pii/S0951833914000586.

Wang, J., Fu, S., Baarholm, R., Wu, J., Larsen, C.M., 2015a. Out-of-plane vortex-induced vibration of a steel catenary riser caused by vessel motions. Ocean Eng. 109, 389–400. http://dx.doi.org/10.1016/j.oceaneng.2015.09.004, URL https://www.sciencedirect.com/science/article/pii/S0029801815004692.

Wang, J., Fu, S., Martin Larsen, C., Baarholm, R., Wu, J., Lie, H., 2017. Dominant parameters for vortex-induced vibration of a steel catenary riser under vessel motion. Ocean Eng. 136, 260–271. http://dx.doi.org/10.1016/j.oceaneng.2017.03.015, URL https://www.sciencedirect.com/science/article/pii/S0029801817301257.

Wang, K., Tang, W., Xue, H., 2015b. Time domain approach for coupled cross-flow and in-line VIV induced fatigue damage of steel catenary riser at touchdown zone. Mar. Struct. 41, 267–287. http://dx.doi.org/10.1016/j.marstruc.2015.02.004, URL https://www.sciencedirect.com/science/article/pii/S0951833915000155.

Williamson, C.H., Govardhan, R., 2004. Vortex-induced vibrations. Annu. Rev. Fluid Mech. 36, 413–455.

Xu, W., Luan, Y., Han, Q., Ji, C., Cheng, A., 2017. The effect of yaw angle on VIV suppression for an inclined flexible cylinder fitted with helical strakes. Appl. Ocean Res. 67, 263–276. http://dx.doi.org/10.1016/j.apor.2017.07.014, URL https://www.sciencedirect.com/science/article/pii/S0141118716305144.

Yin, D., Lie, H., Wu, J., 2019. Structural and Hydrodynamic Aspects of Steel Lazy Wave Riser in Deepwater. J. Offshore Mech. Arct. Eng. 142 (2), http://dx.doi.org/10.1115/1.4045333, 020801. arXiv:https://asmedigitalcollection.asme.org/offshoremechanics/article-pdf/142/2/020801/6511348/omae_142_2_020801.pdf.

Yin, D., Wu, J., Lie, H., Passano, E., Sævik, S., Grytøyr, G., Tognarelli, M., Andersen, T., Igland, R., Karunakaran, D., Gaskill, C., 2022. Wave effects on vortex-induced vibrations of a top-tensioned riser. J. Offshore Mech. Arct. Eng. 145, 1–9. http://dx.doi.org/10.1115/1.4056521.

Zheng, H., Dahl, J.M., Modarres-Sadeghi, Y., Triantafyllou, M.S., 2014. Coupled inline-cross flow VIV hydrodynamic coefficients database. In: International Conference on Offshore Mechanics and Arctic Engineering, Vol. 45400. American Society of Mechanical Engineers, V002T08A087.

Zheng, H., Price, R., Modarres-Sadeghi, Y., Triantafyllou, G.S., Triantafyllou, M.S., 2011a. Vortex-induced vibration analysis (VIVA) based on hydrodynamic databases. In: International Conference on Offshore Mechanics and Arctic Engineering, Volume 7: CFD and VIV; Offshore Geotechnics, pp. 657–663. http://dx.doi.org/10.1115/OMAE2011-50192.

Zheng, H., Price, R., Modarres-Sadeghi, Y., Triantafyllou, G.S., Triantafyllou, M.S., 2011b. Vortex-induced vibration analysis (VIVA) based on hydrodynamic databases. In: International Conference on Offshore Mechanics and Arctic Engineering, Vol. 44397. pp. 657–663.

Zhu, H., Hu, J., Gao, Y., Zhao, H., Xu, W., 2021. Spatial–temporal mode transition in vortex-induced vibration of catenary flexible riser. J. Fluids Struct. 102, 103234. http://dx.doi.org/10.1016/j.jfluidstructs.2021.103234, URL https://www.sciencedirect.com/science/article/pii/S0889974621000177.